

A JVLA, LOFAR, e-Merlin, VLBA and EVN study of RBS 797: can binary SMBHs explain the outburst history of the central radio galaxy?

F. Ubertosi^{1,2}, M. Giroletti³, M. Gitti^{1,3}, N. Biava^{3,4}, E. De Rubeis^{1,3}, A. Bonafede^{1,3}, L. Feretti³, M. Bondi³, L. Bruno^{1,3}, E. Liuzzo^{3,5}, A. Ignesti⁶, and G. Brunetti³

¹ Dipartimento di Fisica e Astronomia, Università di Bologna, via Gobetti 93/2, I-40129 Bologna, Italy
e-mail: francesco.ubertosi2@unibo.it

² Istituto Nazionale di Astrofisica - Osservatorio di Astrofisica e Scienza dello Spazio (OAS), via Gobetti 101, I-40129 Bologna, Italy

³ Istituto Nazionale di Astrofisica - Istituto di Radioastronomia (IRA), via Gobetti 101, I-40129 Bologna, Italy

⁴ Thüringer Landessternwarte, Sternwarte 5, 07778 Tautenburg, Germany

⁵ Italian Alma Regional Center (ARC), Via Piero Gobetti 101, I-40129 Bologna, Italy

⁶ INAF-Padova Astronomical Observatory, Vicolo dell'Osservatorio 5, 35122 Padova, Italy

Received 19 December 2023; Accepted 13 May 2024

ABSTRACT

Aims. The multi-faceted central radio galaxy of the cluster RBS 797 shows several episodes of jet activity in multiple directions. We wish to understand the causes behind these dramatic misalignments and measure the timescales of the successive outbursts.

Methods. We present a multi-frequency (144 MHz – 9 GHz) and multi-scale (5 pc – 50 kpc) investigation of the central radio galaxy in RBS 797, by means of JVLA, LOFAR (with international stations), e-Merlin, VLBA and EVN data. We investigate the morphological and spectral properties of the radio lobes, the jets, and the active core.

Results. We confirm the co-spatiality of the radio lobes with the four perpendicular X-ray cavities discussed in Ubertosi et al. (2021). The radiative ages of the E-W lobes (31.4 ± 6.6 Myr) and of the N-S lobes (32.1 ± 9.9 Myr) support a coeval origin of the perpendicular outbursts, that also have similar *active phase* duration (~ 12 Myr). Based on the analysis of the inner N-S jets (on scales of ≤ 10 kpc), we (a) confirm the S-shaped jet morphology; (b) show the presence of two hotspots per jet with a similar spectral index; (c) estimate the age of the twisting N-S jets to be less than ~ 8 Myr. Based on these results, we determine that jet precession, with period ~ 9 Myr, half-opening angle $\sim 24^\circ$ and jet advance speed $\sim 0.01c$, can explain the properties of the N-S jets. We also find that the synchrotron injection index has steepened from the large, older outbursts ($\Gamma \sim 0.5$) to the younger S-shaped jets ($\Gamma \sim 0.9$), possibly due to a transition from an FR I-like to an FR II-like activity. The e-Merlin, VLBA and EVN data reveal a single, compact core at the heart of RBS 797, surrounded by extended radio emission whose orientation depends on the spatial scale sampled by the data.

Conclusions. We explore several engine-based scenarios to explain these results. Piecing together the available evidence, we argue that RBS 797 likely hosts (or hosted) binary active SMBHs. The detection of a single component in the VLBI data is still consistent with this interpretation, since the predicted separation of the binary SMBHs (≤ 0.6 pc) is an order of magnitude smaller than the resolution of the available radio data (5 pc).

Key words. galaxies: active – Galaxies: clusters: general – Galaxies: clusters: individual: RBS 797 – Galaxies: clusters: intracluster medium – Galaxies: jets – Radio continuum: galaxies

1. Introduction

It is long known that supermassive black holes (SMBHs) can experience multiple phases of activity as Active Galactic Nuclei (AGN) over time (e.g., Saikia & Jamrozy 2009 and references therein). In the case of radio galaxies, the relativistic jets ejected from the central engine can extend from parsec (pc) to tens of kiloparsec (kpc) scales, where radio lobes are usually observed. After a few tens of Myr from the start of the jet activity, the central engine can turn off or greatly reduce its ability to collimate relativistic jets (e.g., Shabala et al. 2008; Turner & Shabala 2015; Morganti 2017; Hardcastle & Croston 2020). The fading radio lobes of sources in this phase usually show a steep radio spectrum and an amorphous shape (Murgia et al. 2011). There are cases in which the SMBH drives a new pair of jets before the previous lobes completely fade. This can result in multiple pairs of radio lobes, with the oldest, most distant pairs having

a steeper radio spectrum (e.g., Saikia & Jamrozy 2009; Saikia 2022; Shabala et al. 2020).

A clear feature of AGN activity traced by restarted jets is the directionality of the successive episodes. A variety of radio sources have so far questioned the idea that SMBH-driven jets are always stable, straight, linear outflows. In the so-called “X-shaped” radio galaxies, two pairs of misaligned lobes are observed. Usually, these objects exhibit a pair of bright, primary jets, and a pair of fainter, secondary lobes (or “wings”) with a steeper spectral index (e.g., Leahy & Parma 1992; Bruno et al. 2019). Additionally, even single pairs of jets can show signatures of wobbling. An S-shaped or Z-shaped morphology traces a curvature or sharp bending of the jet axis (e.g., Lister et al. 2003; Rubinur et al. 2017). In a few other cases, multiple active jets have been observed propagating from a galaxy’s core (e.g., Hudson et al. 2006).

Several scenarios have been invoked to explain misaligned or wobbling jets. The wings of X-shaped radio galaxies may represent either an older episode of AGN activity in a different direction (Dennett-Thorpe et al. 2002; Liu 2004), or backflow of the primary lobe plasma (e.g., Kraft et al. 2005), or the jets from a secondary SMBH (Lal & Rao 2007). Binary SMBHs may also account for the observations of multiple pairs of jets ejected from a compact region (see e.g., the case of 3C 75, Hudson et al. 2006). Ultimately, jets can experience geodetic precession over time (e.g., Fendt & Yardimci 2022). This mechanism is thought to be occurring in a large number of radio galaxies – see e.g., Krause et al. 2019, who found a fraction of $\sim 70\%$ of precessing jets in a complete sample of 3C radio galaxies. Precession may naturally explain the S-shaped morphology of jets (see the cases of e.g., Hydra A Taylor et al. 1990, Cygnus A, Steenbrugge & Blundell 2008; Horton et al. 2020).

Overall, it is still unclear if one of the above scenarios can univocally explain the signatures of the changes in jet axis. Combination of different mechanisms may be invoked. For instance, binary SMBHs can cause jet precession in the active SMBH due to the gravitational interaction of the binary (e.g., Begelman et al. 1980; Krause et al. 2019). In addition, a merger of binary SMBHs may lead to a spin-flip of the merged, more massive SMBH, which would drive jets in a perpendicular direction with respect to the previous outburst (e.g., Merritt & Ekers 2002). The latter case would explain the jet reorientation events characterized by $\sim 90^\circ$ misalignment between the successive jet activities. This holds especially for the radio galaxies with geometrically thick accretion disks, for which the Baarden-Petterson effect is inefficient (e.g., Fragile et al. 2007).

A significant challenge in testing these scenarios arises from the vast range of spatial scales involved, spanning from a few pc to tens of kpc (see also Ubertosi et al. 2024). High-resolution and sensitive radio observations, that can target these widely varying spatial scales, are needed to understand how jets change their orientation over time.

The central radio galaxy of the galaxy cluster RBS 797 (RA 09:47:12.76, DEC +76:23:13.74, $z = 0.354$) represents an exemplary case of multiple and misaligned jet activities. In the innermost 50 kpc, multiple pairs of radio lobes that are misaligned by roughly 90° have been discovered (Gitti et al. 2006, 2013), with the largest and brightest lobes extended in the east (E) - west (W) direction (at ~ 30 kpc from the center), radio fainter lobes in the north (N) - south (S) direction (at ~ 27 kpc from the center) and twin jets heading N-S in the inner ~ 10 kpc. At sub-arcsec resolution, a short observation of the radio core with the European VLBI Network (EVN) at 5 GHz uncovered two compact components separated by ~ 77 pc (Gitti et al. 2013). Combining these findings, Gitti et al. (2013) suggested that either the central SMBH has experienced reorientation events, producing subsequent outbursts in perpendicular directions, or that the brightest cluster galaxy (BCG) hosts a dual AGN, with the two active SMBHs simultaneously launching jets in perpendicular directions (coeval outbursts).

Recently, deep *Chandra* data showed that the AGN activity left numerous imprints on the intracluster medium (ICM) of RBS 797 (Ubertosi et al. 2021, 2023). The detection of strong depressions in the X-ray surface brightness revealed that two perpendicular and equidistant pairs of X-ray cavities were carved in the hot gas at ~ 30 kpc from the center by the perpendicular and equidistant radio lobes (Ubertosi et al. 2021). Additionally, three nested shock fronts driven by the AGN activity were found at distances of 50 kpc, 80 kpc and 130

kpc from the center. The inner shock has the shape of a whole cocoon which surrounds the four perpendicular and equidistant X-ray cavities (Ubertosi et al. 2023). A striking result based on the X-ray data was that the two perpendicular pairs of X-ray cavities are nearly coeval, around 30 Myr old, with an age difference of 1 ± 7 Myr. Ubertosi et al. (2021) concluded that this relatively short outburst interval may be explained either by a nearly coeval activity of active binary SMBHs, or by a rapid reorientation (a few Myr at most) of the jets from a single AGN.

In this work, we present new multi-frequency radio observations of the radio galaxy in RBS 797 from different instruments. We show in Fig. 1 a composite image of RBS 797, created with our new LOFAR and JVLA data. We present the data and the reduction techniques in Section §2. We show our results in Section §3, by focusing on the kpc scale (§3.1), the kpc - pc connection (§3.2), and the pc scale (§3.3). The results are discussed in Section §4, and we summarize our work in Section §5.

Throughout this work we assume a Λ CDM cosmology with $H_0 = 70 \text{ km s}^{-1} \text{ Mpc}^{-1}$, $\Omega_m = 0.3$, and $\Omega_\Lambda = 0.7$, which gives a scale of $4.9 \text{ kpc arcsec}^{-1}$ at $z = 0.354$. We define the radio spectral index α with the following convention: $S_\nu \propto \nu^{-\alpha}$, where S_ν is the flux density at a frequency ν . Unless otherwise stated, uncertainties are reported at 1σ .

2. Radio observations of RBS 797: data reduction

2.1. VLBA, EVN and e-Merlin data reduction

The observations of the BCG in RBS 797 comprise new data from the Very Long Baseline Array (VLBA) using bands L, C and X; the European VLBI Network (EVN) using bands L and C; and the Multi-Element Radio-Linked Interferometer Network (eMerlin) using bands L and C. In the following subsections we describe the observations and the data reduction procedure for the different arrays and frequencies considered. A summary of the observations presented in this article is provided in Tab. 1.

2.1.1. VLBA and EVN data

The radio core of RBS 797 has been observed by the VLBA in L band (1.6 GHz), C band (5 GHz) and X band (8.4 GHz) in phase-referencing mode (project code: BG224, PI: Gitti), with 8 spectral windows (each with a bandwidth of 32 MHz and 128 channels). For all the observing frequencies, the source J0954+7435 has been used as phase calibrator, while the source J2005+7752 has been used as fringe finder. The target has been observed in 4 min scans bracketed by 60 s scans of the phase calibrator, for a total time-on-source of 4 h in L band (60 scans on the target), 40 min in C band (10 scans on the target), and 1 h 20 min in X band (20 scans on the target).

The BCG of RBS 797 has been targeted with the EVN in phase-referencing mode (with 8 spectral windows, each with a bandwidth of 16 MHz and 32 channels). The BCG was observed at 1.6 GHz (project code: EG080-A, PI: Gitti) and at 5 GHz (project code: EG080-B, PI: Gitti), respectively. At both frequencies, J0954+7435 has been used as phase calibrator (observed in scans of 60 s), while 3C345 was observed as fringe finder. The target has been observed in 3m 30s scans for a total time-on-source of ~ 5 h at each frequency.

The strategy adopted to process the data in AIPS (Greisen

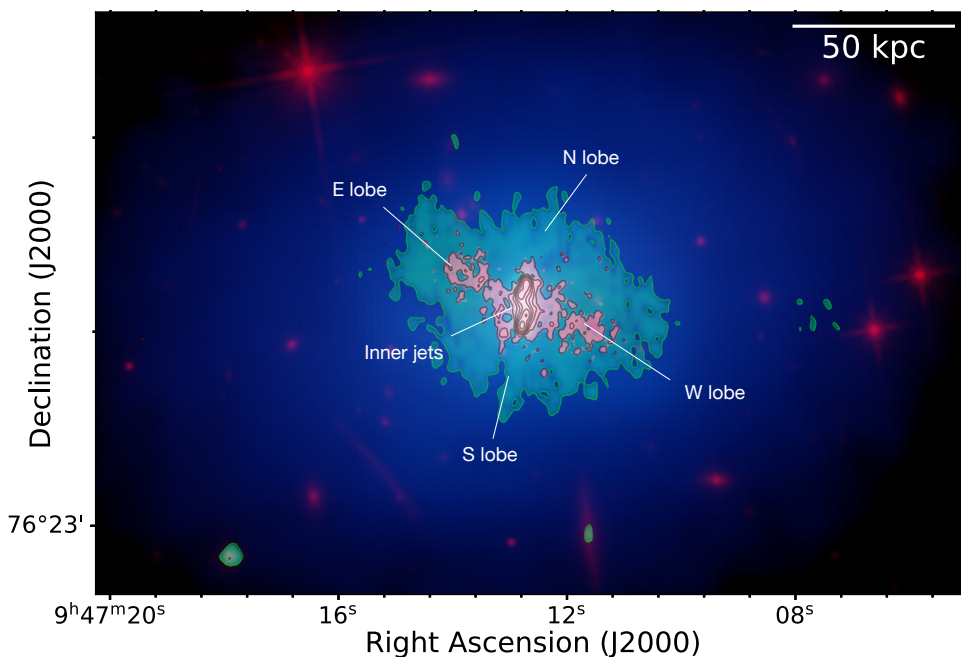


Fig. 1. Composite optical (HST, red), *Chandra* (X-ray, blue), 3 GHz (JVLA, green), 144 MHz (LOFAR-International, pink) image of RBS 797. The structures discussed in this work are labelled. Black contours (described in Fig. 2) outline the 144 MHz emission of the radio galaxy.

2003) is similar for the VLBA and EVN observations. We followed standard reduction techniques, namely:

- Correction of Earth orientation parameters and ionospheric delays (tasks VLBAEOPS, VLBAEOCR). Removal of bad data from system temperatures of the EVN data.
- Correction of delays and amplitudes; we applied digital sampling corrections and removed instrumental delays on phases (VLBACCOR VLBAAMPCL for the VLBA, FRING for the EVN). Then, we calibrated the bandpass (BPASS). At this point, we removed bad data from system temperatures and gain curves of the VLBA observations. To complete the amplitude calibration, we applied the corrections with the task VLBAAMP.
- The time-dependent delays, rates, and phases were corrected by fringe-fitting the data of the calibrator (FRING). To properly correct the visibilities we used an image of the calibrator as a model for fringe-fitting.
- Ultimately, we applied the calibration to the data and averaged the different spectral windows. After editing the final visibilities, self-calibration was attempted only for the L-band data (due to the low flux density of the target), finding however no significant improvement in dynamical range or sensitivity. Images were made in AIPS with the task IMAGR.

We found that supplying an image model during fringe-fitting is crucial when J0954+7435 is used as a calibrator: since the calibrator itself is resolved into a double component, assuming a point source as a model for fringe-fitting results in a bad description of rate and delays (see also §3.3).

When using the software DIFMAP (Shepherd 1997) to fit visibilities with gaussian-like or point-like components, the uncertainties on flux densities were computed as:

$$\delta S_\nu = \sqrt{N_{beam}\sigma_{rms}^2 + (f_\%S_\nu)^2 + \delta_{difmap}^2} \quad (1)$$

where N_{beam} is the ratio between the area within which the flux density is computed and the beam area, σ_{rms} is the local r.m.s. noise, $f_\%$ is the relative uncertainty on the flux density scale (here we assume $f_\% = 10\%$), S_ν is the flux density indicated by the fit and δ_{difmap} is the statistical fit uncertainty (at 1σ confidence level, typically around $5\%S_\nu$) returned by the fit in DIFMAP.

2.1.2. e-Merlin data

The e-Merlin observations of RBS 797 (project code EG080, PI: Gitti) have been performed at L band (1.6 GHz) and C band (5 GHz). At both frequencies, the source J0954+7435 has been used as phase calibrator. The fringe finders were 0319+415 for the L band data and 1331+305 for the C band data. After being passed through the e-MERLIN pipeline (Argo 2015), any problematic data such as spurious signals or data from faulty antennas were identified and flagged.

Images were made in AIPS with the task IMAGR. We found that the best results are achieved by setting the robust parameter to $R = 0$ for the C band data and by selecting a natural weighting for the L band data. Peak and total flux densities (above the $5 \times \sigma_{rms}$ contour) of the radio emission were measured in AIPS at the different frequencies, with the uncertainties being computed as:

$$\delta S_\nu = \sqrt{N_{beam}\sigma_{rms}^2 + (f_\%S_\nu)^2}, \quad (2)$$

where we assume the typical flux density scale uncertainty of $f_\% = 5\%$. By inspecting the radio images, we noticed that there is a shift in the astrometry of the e-Merlin observations, by -38 milliarcseconds in RA and $+3$ milliarcseconds in DEC. In order to properly compare the e-Merlin results with those obtained from other facilities, we corrected the data for this astrometric offset by shifting the images in AIPS.

2.2. JVLA observations and data reduction

We analyze new *Karl Jansky* Very Large Array (JVLA) observations of RBS 797 (Project code 22A-301, PI: Ubertosi) performed with the A array at S band (2 – 4 GHz), C band (4.5 – 6.5 GHz) and X band (8 – 10 GHz). In all observations the source 3C 286 (J0137+3309) was used as the primary flux density calibrator, while J1044+8054 was used as phase calibrator. The data were calibrated in CASA v.6.4.1 (CASA Team et al. 2022) using standard data reduction techniques for continuum calibration¹. Self-calibration of the target is not possible given

¹ See <https://casaguides.nrao.edu/>.

Table 1. Summary of the EVN, VLBA, e-Merlin, JVLA and LOFAR data presented in this work.

PRIMARY DATA					
(1)	(2)	(3)	(4)	(5)	(6)
Telescope	Project Code	Obs. Date	Time on source [h]	Frequency [GHz]	Calibrators
JVLA	22A-301	May 2022	1.5	3.0	3C286, J1044+8054
			0.7	5.5	
			2	9.0	
LOFAR	LC 10_010	June 2018	8	0.144	3C295, L619462
eMerlin	EG080	March 28, 2014	6	1.6	0319+415, J0954+7435
		March 10, 2014	6	5.0	1331+305, J0954+7435
VLBA	BG 224	February 4, 2014	4	1.6	J2005+7752, J0954+7435
			0.7	5.0	
			1.3	8.4	
EVN	EG080	February 26, 2014	5	1.6	3C345, J0954+7435
		March 9, 2014	5	5.0	
COMPLEMENTARY DATA					
EVN	RSG05	May 3, 2013	1	5.0	0133+476, J0954+7435
	RSG07	December 1, 2015	1.5	1.6	J0958+6533, J1027+7428, J0954+7435
VLBA	BE 056	July 8, 2014	0.3	5.0	4C 39.25, J1044+8054

Notes. We separate the primary, sensitive data (that we use to derive the main results) from the shorter-observing time complementary data (that we use to verify the results based on primary data). (1) Name of the radio telescope; (2) project code; (3) date of the observations; (4) time spent on the target source RBS 797; (5) observing frequency; (6) Name of the calibrators.

its relatively low flux density (peak flux density of $1 - 2$ mJy at GHz frequencies, see Tab. 2). Nonetheless, the noise in our images is close to the theoretical expected one.

The data were imaged in CASA using the task `tclean`, and testing different weighting combinations. For the S band (3.0 GHz) data, we find that an image made with `robust = 0` highlights the jet structure in the inner 15 kpc, while an image made with `robust = 2` recovers extended emission on larger scales, reaching the lobe of the radio galaxy. For the data at C and X bands, the images that best capture the radio morphology are obtained by setting `robust = 0`. Different choices of weighting schemes were tested, but the image quality or the total recovered flux density did not demonstrate any significant variations. The images are shown in Fig. 2 (panels *a*, *b*, *c*, *d*). We measured the peak and total flux density (above the $5 \times \sigma_{\text{rms}}$ contour) of the radio emission at the different frequencies. The uncertainties were computed as in Eq. 2, assuming the typical flux density scale uncertainty of 5%.

2.3. LOFAR long-baseline observations

RBS 797 has been observed by the LOw Frequency ARray (LOFAR, van Haarlem et al. 2013) in 2018 (Project code: LC 10_010, PI: Bonafede). The observations used the HBA antennas and the same setup of the LOFAR Two Meter Sky Survey (LoTSS, e.g., Shimwell et al. 2022), with 22 core stations, 13 remote stations, and 13 international stations. The source has been

observed between 120 MHz and 168 MHz (central frequency 144 MHz) for 8h, using the calibrator 3C295.

To calibrate the data (including the international stations) we followed the prescriptions detailed in Morabito et al. (2022)² using the HOTCAT High Performance Computing cluster at INAF Trieste (Taffoni et al. 2020; Bertocco et al. 2020). The data were first passed through the `Pre-factor3` software package (van Weeren et al. 2016; Williams et al. 2016; de Gasperin et al. 2019), which uses the calibrator source to derive the corrections for polarization alignment, Faraday rotation, bandpass, and clock offsets. Then, a first set of phase calibration solutions for the core and remote stations (derived using a sky model of the field from the TGSS survey, Intema et al. 2017) are added to the calibrator solutions.

The LOFAR-VLBI pipeline is subsequently used to calibrate the international stations. This requires to select a bright and compact source separated by less than 1 degree from the target from the Long-Baseline Calibrator Survey (LBCS, Jackson et al. 2022). We derived the solutions for the international stations using L619462, which is located at 0.56° from the target RBS 797. After splitting out the target visibilities, the solutions from the delay calibrator were applied to the target.

To improve the image quality, self-calibration was performed on the target using the Default Preprocessing Pipeline DPPP (van Diepen et al. 2018) to find the solutions, and WSClean v3.2 (Ofringa et al. 2014) to obtain images (see also van Weeren et al.

² See also <https://lofar-vlbi.readthedocs.io>.

Table 2. Image parameters of the EVN, VLBA, e-Merlin, JVLA and LOFAR data used in this paper.

(1)	(2)	(3)	(4)	(5)	(6)	(7)	(8)	(9)	(10)
Telescope	Project Code	Frequency [GHz]	Robust	Beam [mas]	P.A. [°]	σ_{rms} [$\mu\text{Jy}/\text{beam}$]	Peak [mJy/beam]	S_{ν} ($5\sigma_{\text{rms}}$) [mJy]	Figure
JVLA	22A-301	3.0	2	900×900	0	5.0	2.07	10.09 ± 0.50	Fig. 2a
		3.0	0	590×400	5.7	6.0	1.69	4.89 ± 0.24	Fig. 2b
		5.5	0	388×250	15.4	5.5	1.57	2.97 ± 0.15	Fig. 2c
		9.0	0	230×200	-4.5	3.0	1.36	2.07 ± 0.10	Fig. 2d
LOFAR	LC 10_010	0.144	0	360×250	170.4	40	13.0	134.4 ± 26.9	Fig. 2
eMerlin	EG080	1.6	5	150×150	0	14	1.51	3.44 ± 0.20	Fig. 6
		5.0	0	35×35	0	20	0.50	0.94 ± 0.08	
VLBA	BG 224	1.6	0	6.3×4.6	82.3	25	0.61	0.94 ± 0.09	Fig. 7
		5.0	0	2.2×1.4	-80.9	30	0.38	0.47 ± 0.05	
		8.4	0	1.3×0.9	-86.4	30	0.39	0.40 ± 0.05	
EVN	EG080	1.6	0	9.1×6.7	-46.9	30	1.37	1.65 ± 0.17	Fig. 7
		5.0	0	2.6×1.6	-62.6	15	0.51	0.70 ± 0.07	
	RSG05	5.0	0	7.2×5.2	-13.9	20	0.68	0.84 ± 0.09	-
	RSG07	1.6	0	29.1×23.9	-36.4	64	1.50	1.91 ± 0.22	-

Notes. (1) Name of the radio telescope; (2) project code; (3) observing frequency; (4) robust parameter used during imaging; (5) beam major and minor axes; (6) beam position angle; (7) r.m.s. noise; (8) peak flux of the image; (9) total flux density within the $5\sigma_{\text{rms}}$ contour; (10) corresponding figure. The weighting obtained with a specific absolute value of the robust parameter depends on the processing software: the parameter refers to the CASA task `tclean` for the JVLA data, to the WSClean software for the LOFAR data, and to the AIPS task `IMAGR` for the e-Merlin, VLBA and EVN data. The EVN project RSG05 had already been published in Gitti et al. (2013), and a preliminary JVLA image at 3.0 GHz from project 22A-301 (with resolution $0.9'' \times 0.8''$) was presented in Ubertosi et al. 2023.

2021). We performed three cycles of self-calibration solving for total electron content (TEC) and phase, and a final cycle of amplitude corrections. To correct for possible offset in the absolute flux density scale (see Shimwell et al. 2022), we compared the flux density of the unresolved delay calibrator between the LOFAR-VLBI image and the $6''$ LOFAR survey image, finding a correction factor of 1.61 that was applied to the images. We computed the uncertainties on the flux densities using Eq. 2 and assuming a 20% uncertainty on the absolute flux density scale to account for uncertainties in the above correction factor of LOFAR-VLBI data (see also Mahatma et al. 2023). This conservative choice is higher than the typical 10% assumed for LOFAR data (Shimwell et al. 2022). The angular resolution of the final image is of $0.36'' \times 0.25''$, and the r.m.s. noise is $\sigma_{\text{rms}} = 40 \mu\text{Jy}/\text{beam}$. Images with a resolution down to a $\sim 1''$ beam were tested, but no improvement was found. The missing uv-coverage between baselines of $50\text{k}\lambda - 75\text{k}\lambda$ (Morabito et al. 2022) prevents us from trading off high spatial resolution for improved image sensitivity (see also §3.1.3). We point the reader to Bonafede et al. (2023) for a study of diffuse emission in RBS 797 using sensitive, low-resolution (beam of $\sim 4''$) LOFAR data.

2.4. Complementary archival data

To complement the analysis of the targeted, deep observations presented above we consider additional archival data from different facilities. We use two EVN snapshot observations, one at 1.6

GHz (project RSG07), and the other at 5 GHz (project RSG05, published in Gitti et al. 2013). We also use a snapshot VLBA observation at 5 GHz to understand if time variability is present in RBS 797 (project BE056, PI Edge; see §3.4). We reduced the data with the same approach presented in §2.1. A summary of the observations is reported in Tab. 1 and 2.

Additionally, we relied on archival VLA data at 1.4 GHz (arrays A, B, and C; see Gitti et al. 2006; Doria et al. 2012), and at 4.8 GHz (arrays A and B, see Gitti et al. 2013). These data were used in combination with our new JVLA and LOFAR observations to measure the spectral properties of the radio galaxy (see §3.1.3).

3. Results

Given the large difference in physical scales to which the employed data are sensitive (from tens of kpc down to tens of pc), in this section we present our results by progressively zooming into the radio core of RBS 797. Starting from the kpc scales, we present the new observations performed with the JVLA and LOFAR telescopes. Then, we probe the connection between the kpc and pc scales using the e-Merlin observations. Ultimately, we present the images obtained from the EVN and VLBA data, that allow us to peer into the pc scales.

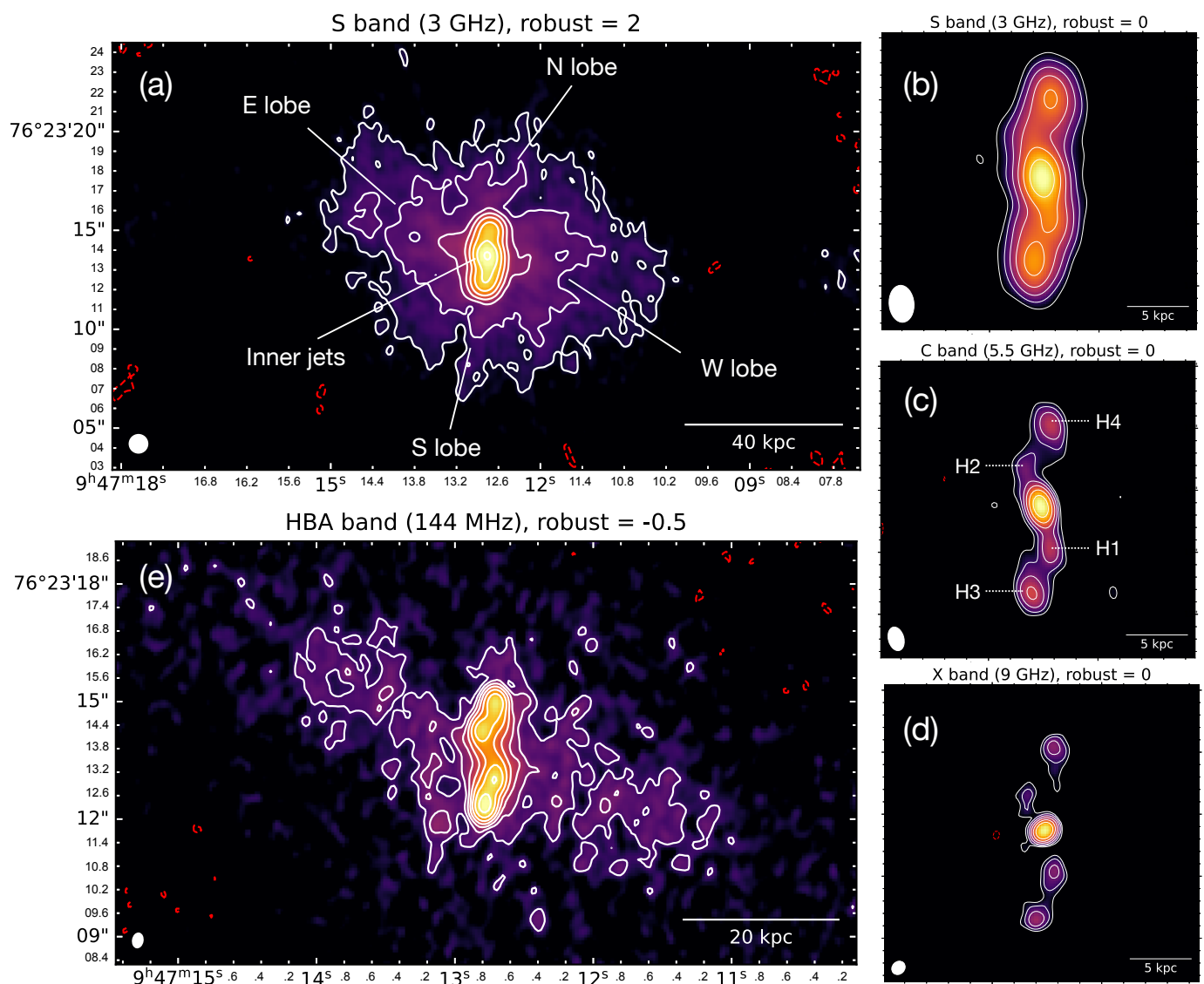


Fig. 2. Final JVLA and LOFAR maps of RBS 797. (a) 3 GHz JVLA image at $0.9''$ resolution, obtained by setting the robust parameter to 2. (b), (c), (d) 3 GHz, 5.5 GHz, and 9 GHz JVLA images obtained by setting robust = 0. The beam sizes are $0.59'' \times 0.40''$ at 3 GHz, $0.39'' \times 0.25''$ at 5.5 GHz, and $0.23'' \times 0.20''$ at 9 GHz. (e) 144 MHz LOFAR image with the International Stations at $0.36'' \times 0.25''$ resolution, obtained by setting robust = -0.5 . In each panel, the beam is shown with a white circle in the bottom left corner. In panels (a) and (e), contours start at $3\sigma_{\text{rms}}$ and increase by a factor of 2; in panels (b), (c), and (d), contours start at $5\sigma_{\text{rms}}$ and increase by a factor of 2. The first negative contour ($-3\sigma_{\text{rms}}$ or $-5\sigma_{\text{rms}}$) is plotted in dashed red. See Tab. 2 for the σ_{rms} noise levels of the images. Structures discussed in this work are labelled.

3.1. The kpc scale

3.1.1. Radio galaxy morphology

We show in Fig. 2 the images obtained from the JVLA data at 3 GHz (panels *a* and *b*), 5.5 GHz (panel *c*), and 9 GHz (panel *d*) and the image obtained from the LOFAR-VLBI data at 144 MHz (panel *e*). The 3 GHz JVLA image obtained with robust = 2 unveils the full morphology of the radio galaxy at a resolution of $0.9''$ (Fig. 2*a*; a preliminary image was already presented in Ubertosi et al. 2023). This image allows one to appreciate the multi-faceted morphology of the radio galaxy in RBS 797, with its perpendicular pairs of radio lobes, extending for ~ 50 kpc, that fill all the four X-ray cavities in the ICM (see also Ubertosi et al. 2021), and the inner north-south jets of the AGN.

Such north-south inner jets, with a distinctive S-shape, are better visible in the maps at 3.0 GHz ($\sim 0.5''$ resolution), 5.5 GHz ($\sim 0.3''$ resolution), and 9 GHz ($\sim 0.2''$ resolution) shown in

the right panels. The jets extend for $1.8''$ (~ 9 kpc) on each side of the core. We identify a total of four bright hotspots, two on each sides of the nucleus and symmetric with respect to the core. The connection between the inner jets and the larger, diffuse radio emission is clearer in the LOFAR image with international stations ($\sim 0.3''$ resolution). At 144 MHz the central emission is dominated by the S-shaped jets, while the core is not visible (Fig. 2, panel *e*). The brightest, innermost part of the extended east-west lobes is also visible at $\sim 3 - 6 \sigma_{\text{rms}}$. The emission is nearly perpendicular to the north-south jets, and it is detected up to a distance of $\sim 6''$ (~ 29 kpc) on each side of the core. The symmetric morphology of the inner north – south jets strongly suggests that the whole structure mainly lies in the plane of the sky, i.e. the angle between the jet axis and the line of sight is nearly 90° . We note that the two southern hotspots are brighter by a factor $\sim 1.2 - 1.7$ than the northern ones (from 144 MHz to 9 GHz). If this is caused by relativistic effects (e.g. Pearson 1996), then the southern jet would be the approaching jet and

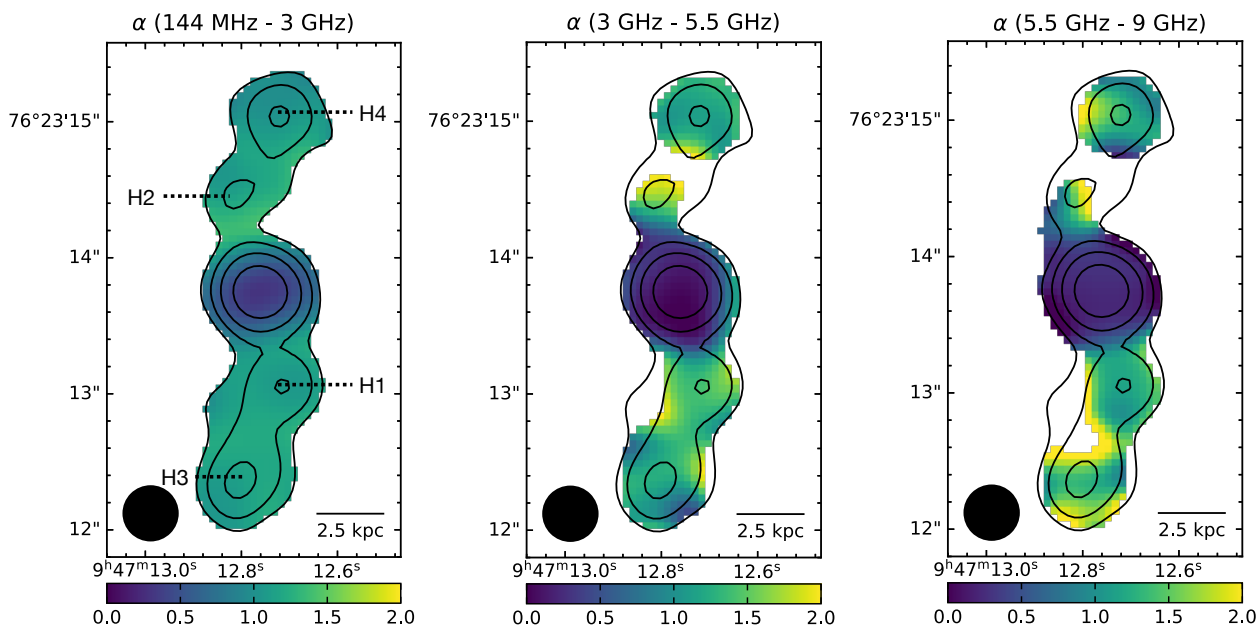


Fig. 3. Spectral index maps of the inner jets. The maps are between 144 MHz and 3 GHz (left), 3 GHz and 5.5 GHz (center), 5.5 and 9 GHz (right), displayed with a matching color-scale of $0 \leq \alpha \leq 2$. Contours from the 3 GHz map used for the spectral index are overlaid. The relative uncertainty on the spectral index range between 2.5% - 15% (144 MHz - 3 GHz), 6% - 15% (3 GHz - 5.5 GHz), 7% - 30% (5.5 - 9 GHz). Structures discussed in this work are labelled.

the northern jet the receding one. From the jet/counter-jet ratio, we estimate an upper limit to the inclination angle of $i \leq 84^\circ$. This supports the above argument of the jets mainly lying in the plane of the sky.

We note the absence in the 5.5 GHz JVLA map of the faint E-W jets detected at $\sim 4 - 5\sigma_{\text{rms}}$ in the narrow-band 4.8 GHz VLA images of Gitti et al. (2006, 2013). The small E-W jet-like features in Gitti et al. (2013) may represent the brightest patch of the diffuse, large lobe emission that is visible in the 3 GHz (robust = 2) and in the LOFAR maps. Given the lower sensitivity to extended emission of the robust = 0 JVLA maps, such diffuse components are likely resolved out. Alternatively, it is possible that the features in the old VLA maps (Gitti et al. 2006, 2013) were caused by serendipitous noise structures near the core.

3.1.2. Spectral properties of the inner jets

The spectral properties of the radio emission provide useful information on the history of the AGN outbursts. The available JVLA and LOFAR data with similar resolution enable a spatially-resolved spectral study of the north – south jets over nearly two orders of magnitude in frequency (144 MHz – 9 GHz). To this end, we produced images at the four frequencies by matching the uv-range of the data (15.2 k λ – 481.9 k λ , corresponding to angular scales of 13.6'' – 0.4'') and selecting a uniform weighting scheme. The resulting maps have a resolution of 0.4''.

We show in Fig. 3 the maps of spectral index between 144 MHz – 3 GHz (*left*), 3 GHz – 5.5 GHz (*center*), and 5.5 GHz – 9 GHz (*right*). Across the four frequencies, the core spectral index remains fairly flat. Using a beam-sized region, and treating the LOFAR flux density as a limit (the core is undetected in the 144 MHz image), we fitted the core measurements with a power-law, finding $\langle \alpha_{\text{core}} \rangle = 0.19 \pm 0.02$.

The spectral index along the jets is steeper than in the core, and across the four frequencies ranges between $0.9 \leq \alpha \leq 2$. The spectral index distribution is not uniform, but we note a flatter α at the center of the hotspots, and a progressive steepening behind them. This is consistent with particles being accelerated at the hotspots of jets, which have a spectral index at lower frequencies that is close to the injection index (e.g., O’Dea et al. 2009). The flatter hotspot spectrum is evident from Fig. 4 (*left panel*). In this figure we compare the core radio spectrum, the total hotspots spectrum (obtained by summing the flux density within beam-sized regions), and the spectrum of the trailing plasma in the remaining area. The difference between the hotspots and the trailing plasma becomes more evident at increasing frequencies. Such spectral steepening at GHz-frequencies is likely caused by radiative losses from particle ageing. Specifically, the synchrotron energy losses of a population of electrons are faster at higher energy, producing increasingly curved radio spectra over time. The time t that has passed since injection can be recovered from the radio spectrum by measuring the break frequency, ν_b (which describes the increasing curvature), and the magnetic field, B , by considering that (e.g., Slee et al. 2001):

$$t = 1.6 \times 10^3 \frac{B^{0.5}}{(B^2 + B_{\text{CMB}}^2)} \frac{1}{[\nu_b \times (1+z)]^{0.5}} \text{ Myr}, \quad (3)$$

where z is the redshift and $B_{\text{CMB}} = 3.25(1+z)^2 [\mu\text{G}]$.

To investigate the spectral ageing of the relativistic particles, we derived a radiative age map of the inner jets by combining the images at the different frequencies (144 MHz, 3 GHz, 5.5 GHz and 9 GHz). We used the Broadband Radio Astronomy Tools software (BRATS, Harwood et al. 2013), that can fit ageing models to 2D maps of radio emission. We tested two radiative age models that consider synchrotron and inverse-Compton losses, where the electron population has a continuously isotropized pitch angle distribution. The JP model (Jaffe & Perola 1973) uses a constant magnetic field, while the Tribble model (Tribble 1993) assumes a Gaussian distribution for the magnetic field.

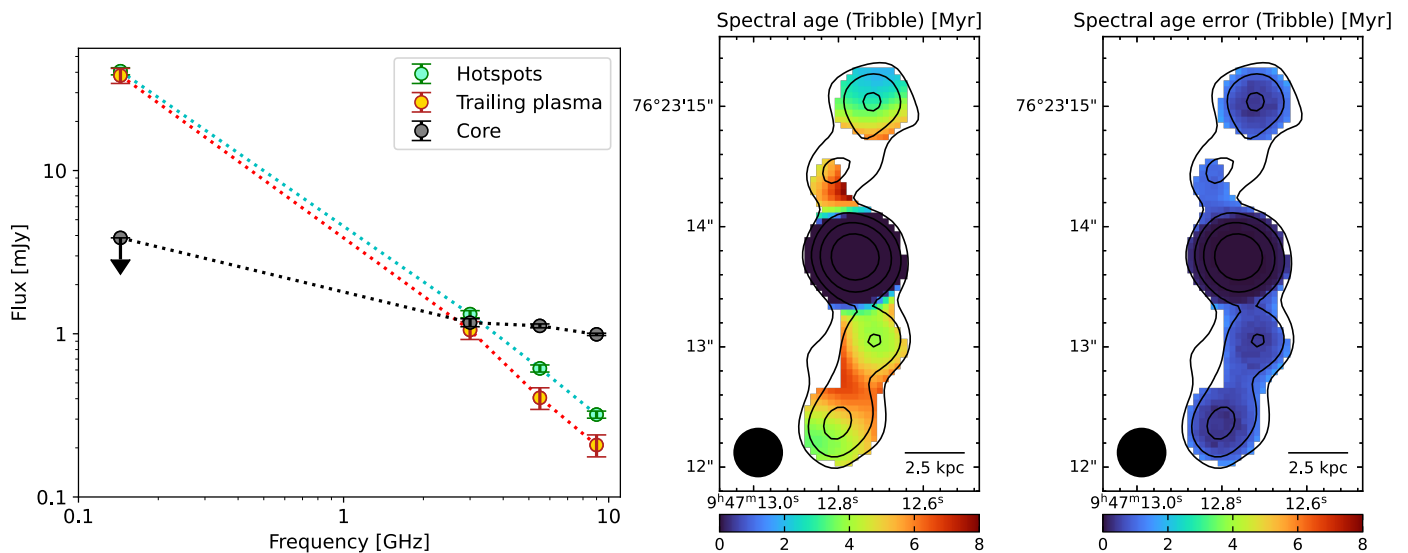


Fig. 4. Spectra and radiative ages of the inner jets. *Left panel:* Radio spectrum of the different components (core, hotspots, and trailing regions) of the north - south radio emission on kpc scales. The total radio spectrum of the hotspots has been obtained by summing the flux densities of the four hotspots within beam-sized regions. The 144 MHz flux density of the core is interpreted as an upper limit, since the core is not detected at low frequency (see §3.1.2 for details). Note that the dotted lines connecting the points do not represent fits to the spectrum. *Right panel:* Spectral age map (assuming a Tribble model) and associated uncertainty map. Contours from the 3 GHz map used for the spectral index computation (Fig. 3) are displayed on top of the image. The beam is shown in the bottom left corner. See §3.1.2 for details.

We refer the reader to Hardcastle (2013); Harwood et al. (2013) and to the BRATS Cookbook³ for details on the equation of the above ageing models.

The input parameters for the JP and Tribble models are the magnetic field B and the injection index Γ . The magnetic field has been estimated from the 3 GHz map adopting equipartition assumptions (e.g., Govoni & Feretti 2004). We measured a k -corrected radio power of $(1.79 \pm 0.09) \times 10^{24}$ W/Hz from a prolate ellipsoid of major semi-axis $1.83''$, minor semi-axis $0.66''$, and position angle 90° from the west axis (volume of 3.34 arcsec³, or 392.3 kpc³). Using these parameters and assuming an energy ratio of protons to electrons of 1, we derived an equipartition magnetic field of $B_{eq} = 16 \pm 2$ μ G along the ~ 8 kpc - long jets, and we fixed $B = B_{eq}$. Using the findinject task of BRATS and excluding the region of the core (e.g., Brienza et al. 2020), we found an injection index $\Gamma = 0.9$. Typical values can range between $0.5 - 0.8$ (e.g., Carilli et al. 1991), with steeper indices (up to 1.2) found for cluster - central powerful radio sources (e.g., Harwood et al. 2015).

Fitting the two models to the data resulted in the Tribble model having a lower reduced- $\chi^2 = 1.12$ than the JP model ($\chi^2 = 1.31$). Moreover, the two models give consistent best-fit radiative ages. As a note of caution, we report that fixing the magnetic field to the minimum energy loss field (e.g., de Gasperin et al. 2017) value of $B = 3.4$ μ G (Ubertosi et al. 2021) returns radiative ages that are larger than those obtained by adopting $B = B_{eq}$ by $\sim 30\%$, but consistent within $\sim 2\sigma$. Considering this, and the fact that the Tribble model describes a more general case, we adopt this one as the best fit to the radio image. We show in Fig. 4 (*right panel*) the radiative age map and the associated uncertainty map.

Our wide frequency range, which extends over three orders of magnitude, ensures high accuracy on the fitted radiative ages, that have relative uncertainties between 5% and 25%. The core has a radiative age consistent with zero, which is in agreement

with its spectral index being below the injection index. The jets have radiative ages that range between 2 - 7 Myr, with the hotspots being younger than the trailing radio plasma behind and around them. In particular, the average age of the hotspots is $t_{rad,H^*} = 4.4 \pm 0.5$ Myr, compared to the average (hotspot-removed) jet age of $t_{rad,j} = 5.8 \pm 0.3$ Myr (see Tab. 3).

The typical model of an ageing radio galaxy would predict the lower ages to be found in the hotspot of each lobe (or in the proximity of the jet termination point), with the surrounding plasma displaying larger radiative ages (e.g., Carilli et al. 1991). In the case of RBS 797 we instead see two bright spots for each jet, and a similar radiative age across the four hotspots. This supports the presence of multiple acceleration sites along the jets, not only the terminal ones. We further discuss this finding in §4.

3.1.3. Spectral properties of the perpendicular lobes

An open question on RBS 797 is which pair of the perpendicular radio lobes and corresponding X-ray cavities is older. Based on deep X-ray observations, Ubertosi et al. (2021) determined that the two pairs of X-ray cavities are ≈ 30 Myr old, and they put an upper limit on the age difference between the two outbursts of ≤ 10 Myr. Ubertosi et al. (2021) also attempted a spectral modeling of the lobes radio spectra, finding a tentative upper limit on the radiative age of $t_{EW} \leq 37$ Myr and $t_{NS} \leq 38$ Myr. However, given the availability at the time of two frequencies only (1.4 GHz and 4.8 GHz old VLA data), no conclusive result could be obtained.

With the new LOFAR and JVLA data at 144 MHz and 3 GHz, respectively, in combination with the old VLA data published in Gitti et al. (2006, 2013), we can now perform a detailed spectral modeling of the radio lobes. Flux densities have been measured from maps obtained by setting a common uv-coverage (4.2 k $\lambda - 175.4$ k λ), using uniform weighting, and a matching resolution of $1.5''$.

³ <https://www.askanastronomer.co.uk/brats/>

Table 3. Summary of spectral age fitting of the different structures of the radio galaxy in RBS 797.

(1)	(2)	(3)	(4)	(5)	(6)	(7)	(8)	(9)
Structure	Component	Model	B [μG]	ν_b [GHz]	Γ	t_{age} [Myr]	t_{on} [Myr]	t_{off} [Myr]
Inner jets	Hotspots	Tribble	16 ($=B_{eq}$, fixed)	–	0.9 (fixed)	4.4 ± 0.5	–	–
	Trailing plasma			–		5.8 ± 0.3	–	–
Outer lobes	E – W	CI-off	3.4 ($=B_{min}$, fixed)	3.1 ± 0.2	0.54 ± 0.04	31.4 ± 6.6	11.4 ± 2.4	20.1 ± 4.2
	N – S			3.0 ± 0.3	0.54 ± 0.05	32.1 ± 9.9	12.8 ± 4.0	19.3 ± 6.0

Notes. In the first row, we report the summary of the Tribble model fit to the inner jets of the radio galaxy (see Fig. 4 and §3.1.2). Note that the fitting has been performed in two dimensions, and the *Hotspots* and *Trailing plasma* components are average estimates derived from the 2D maps shown in Fig. 4. In the second row, we report the best fit parameters for the CI-off model fitted to the radio spectrum of the E-W and N-S lobes of RBS 797 (see Fig. 5 and §3.1.3). In this second case, the fitting has been performed over the integrated spectra of the radio lobes (bottom panel of Fig. 5). (1) Structure of the radio galaxy; (2) sub-component of the structure; (3) model used to fit the synchrotron spectra; (4) magnetic field adopted during the fitting procedure; (5) break frequency of the spectrum; (6) injection index; (7) total age of the radio emission; (8) active phase duration (CI-off model only); (9) remnant phase duration (CI-off model only).

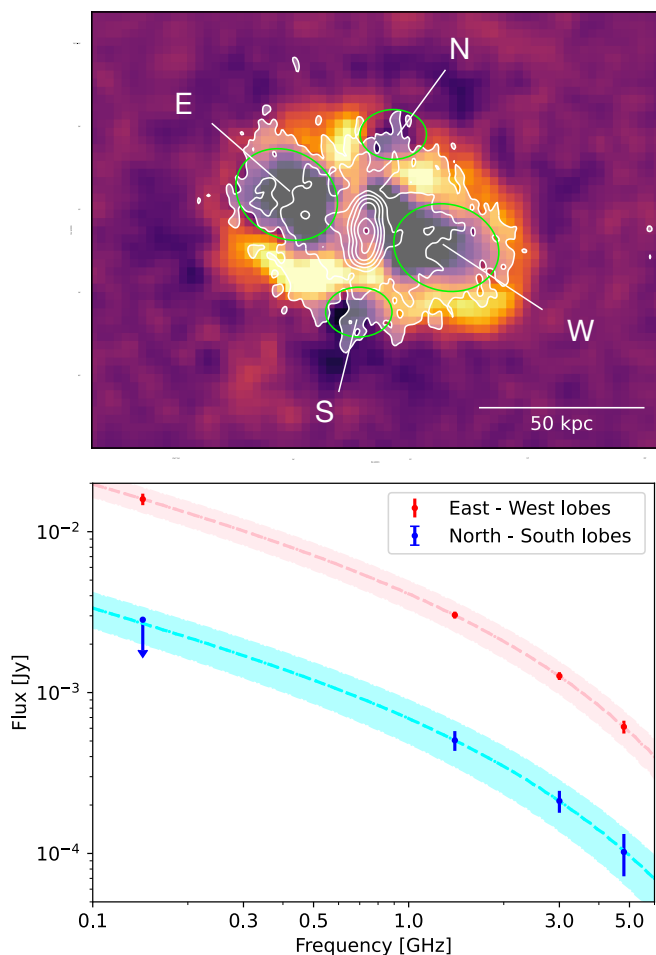


Fig. 5. Spectral age study of the perpendicular radio lobes. *Top:* Residual *Chandra* image of RBS 797, with overlaid white contours from the JVLA 3 GHz image of Fig. 2. The X-ray cavities described in Ubertosi et al. (2021) are shown with green ellipses and labelled. *Bottom:* Spectrum of the radio emission from the E-W and N-S cavities (see regions in top panel) in RBS 797, fitted with a CI-off model (see §3.1.3 for details). Colored areas show the 1σ uncertainties on the best-fit model.

We note that the missing uv-coverage in the LOFAR data between baselines of roughly $50k\lambda - 75k\lambda$ limits the sensitiv-

ity to extended emission between scales of $2'' - 4''$ (Morabito et al. 2022). For this reason, for the fainter N-S lobes we only have upper limits on the extended emission from the LOFAR data. Similarly, the 4.8 GHz VLA data detect the lobes only at $\sim 3\sigma_{rms}$. As the signal-to-noise would be too low, we cannot derive spatially-resolved spectral measurements, but we can obtain integrated values for each component. To this aim, we measured the flux densities within the regions defining the X-ray cavities (see Fig. 5, top panel). The resulting spectrum of the E-W lobes and the N-S lobes is shown in Fig. 5, bottom panel.

We note that the spectra of the two lobe pairs follow a similar steepening trend towards higher frequencies, with the N-S lobes being a factor of approximately 5 fainter than the E-W lobes. Interestingly, the E-W cavities are also roughly five times more powerful than the N-S cavities, in agreement with the already known scaling between radio and mechanical powers (e.g. Bîrzan et al. 2008; Cavagnolo et al. 2010; O’Sullivan et al. 2011).

Using the software SYNCHROFIT (Quici et al. 2022), which is suited to analyze integrated spectra, we fitted the two spectra using a continuous injection with a remnant phase model (CI-off, Komissarov & Gubanov 1994). With respect to the JP or Tribble models (that are based on a single injection event), the CI-off model describes an electron population that is injected at a constant rate for a duration t_{on} (the active phase), then the nuclear activity shuts down and the electrons age for a time t_{off} (the remnant phase). During the active phase, the radio spectrum has a curved shape, described by a break frequency ν_b , which depends on the total age of the radio source as in Eq. 3. For $\nu \geq \nu_b$, the spectral index is $\Gamma + 0.5$, where Γ is the injection spectral index. Then, at a time t_{on} , the source injecting fresh electrons switches off and the synchrotron-emitting electrons continue ageing for a time t_{off} (the remnant phase). This produces a second break frequency in the spectrum, $\nu_{b,2}$, defined as:

$$\nu_{b,2} = \nu_b \times \left(\frac{t_{age}}{t_{off}} \right) = \nu_b \times \left(\frac{t_{off} + t_{on}}{t_{off}} \right). \quad (4)$$

For details on this model and the corresponding equations, see Komissarov & Gubanov (1994); see also Biava et al. (2021) for a similar application.

The choice of the CI-off for the lobes of RBS 797 is physically motivated by the fact that the diffuse lobe emission is not currently powered by active jets, as the most recent activity is in the

north - south direction and on smaller scales (see §3.1). Indeed, we found that single injection models are unable to correctly fit the data.

The model requires the redshift ($z = 0.354$) and the magnetic field to be fixed, and returns the injection index Γ , the break frequency ν_b (which is related to the total age of the source, $t_{off} + t_{on}$), and the remnant fraction ($t_{off}/(t_{off} + t_{on})$). In the region of the lobes, we measure an equipartition magnetic field that ranges between $3.2 \mu\text{G}$ to $4.2 \mu\text{G}$ depending on the selected region. For comparison, the minimum energy loss field is $B_{min} = 3.4 \mu\text{G}$. Given the similarity between these values, we adopted a common magnetic field $B = B_{min}$ during fitting.

As it is possible to see from Fig. 5, the CI-off model provides a good description of the integrated radio spectrum of the E-W and N-S lobes ($\chi^2/\text{d.o.f.}$ of 1.03 and 1.09, respectively). The best fit parameters for the E-W and N-S lobes are reported in Tab. 3. We find that the spectra of the two pairs of lobes are described by similar parameters. First, we note that the total age of the radio lobes (~ 30 Myr) is in good agreement with the age of the X-ray cavities (Ubertosi et al. 2021) and of the corresponding weak shock in the ICM (Ubertosi et al. 2023). Second, the similar total age, active phase duration, and remnant phase duration of the E-W and N-S lobes suggest that it is difficult to determine which outburst is younger. Rather, these results support a coeval origin of the two pairs of radio lobes, as suggested before from the X-ray data. We discuss these results in the framework of radio activity in RBS 797 in §4.

3.2. From the kpc to the pc scale

We present in Fig. 6 the images obtained from the e-Merlin observations of RBS 797 at L band (1.6 GHz) and C band (5 GHz). Tab 2 reports the parameters used during imaging and the corresponding image properties.

The 1.6 GHz image shows the inner jet structure with a resolution of $0.15''$ (~ 0.7 kpc). In particular, the core is visible at the center of the image (with an unresolved flux density of 1.51 mJy), and the jet emission mainly coming from the four hotspots is recovered on larger scales (total flux density 3.4 mJy). This image represents the highest resolution view of the ~ 8 kpc long jets of RBS 797, and confirms the S-shaped morphology revealed by the JVLA and LOFAR images of Fig. 2.

The 5 GHz image has a resolution of $0.035''$ (~ 170 pc). The emission is resolved into two components, with the brighter one (labelled A) centered on the position of the radio core (RA, DEC = 09:24:12.76, +76:23:13.74) and the fainter one (labelled B) located at a distance of $0.05''$ (~ 250 pc) westward. Although the dynamic range of the 5 GHz e-Merlin image is relatively small (around 25), the two components are detected at more than $5\sigma_{\text{rms}}$, up to $\sim 28\sigma_{\text{rms}}$ for the brighter component and $\sim 20\sigma_{\text{rms}}$ for the fainter one. Using the software DIFMAP we fitted the combination of two Gaussian components to the uv data. We found that A is described by a Gaussian with flux density $S_A = 0.55 \pm 0.04$ mJy and a nominal deconvolved major axis of 1.1 ± 0.1 mas (5.4 ± 0.5 pc). This is a factor of ~ 32 smaller than the beam size, indicating that the component is unresolved. The second component is described by a Gaussian with flux density $S_B = 0.38 \pm 0.04$ mJy and a deconvolved major axis of 10.2 ± 1.4 mas (51 ± 7 pc). This is a factor ~ 3 smaller than the beam size, possibly suggesting that the component may be extended.

Given its position, compactness, and flux density, we identify the brighter component, A, with the central engine of RBS 797. The second component is more difficult to interpret. This fainter component, B, could arise from a second SMBH in the BCG of

RBS 797, which has been argued as a possible explanation for the multiple and misaligned outbursts in this cluster Gitti et al. (2006, 2013); Ubertosi et al. (2021). Alternatively, it could represent remnant extended emission from the large scale outburst (see §3.1), since its relative position with respect to the core matches the orientation of the large east – west lobes of the radio galaxy (see Fig. 2). This alternative interpretation would be in agreement with its possible classification as an extended component from the DIFMAP fitting procedure. We also considered the possibility that this feature would be part of the southern approaching jet, however this seems hard to reconcile with the position angle of the component S1 detected with VLBA (see next section). We exploit the information from the VLBA and EVN data presented in the next section to discuss which scenario is more plausible.

3.3. The pc scale

We show in Fig. 7 the VLBA images at 1.6 GHz, 5 GHz and 8.4 GHz (top panel), and the EVN images at 1.6 GHz and 5 GHz (bottom panel) at mas resolution. The parameters of the images are reported in Tab. 2. From these images we identify a single source at the phase center; the emission appears unresolved, with the exception of the VLBA 1.6 GHz image, where a faint extension is visible south of the peak.

We used DIFMAP to identify components from the uv-data and measure their flux densities. Based on this analysis, we found that the VLBA data at 1.6 GHz are well described by the combination of two components: a bright one (A, 0.75 ± 0.09 mJy) coincident with the radio peak, and a fainter one (S1, 0.27 ± 0.04 mJy) at a distance of 12 mas (~ 60 pc) south of A. We observe that the position angle of the jet-like component S1 matches the jet orientation on JVLA and LOFAR scales (see Fig. 2). Additionally, the one-sidedness of the jet is consistent with the possible interpretation presented in §3.1.2 of the southern jet being the approaching one. The VLBA data at higher frequencies are described by a single, unresolved component (coincident with A), with a flux density of 0.47 ± 0.05 mJy (at 5 GHz) and 0.40 ± 0.05 mJy (at 8.4 GHz).

The EVN data at 1.6 GHz is fitted with a single component with a flux density of 1.65 ± 0.17 mJy, that we identify as A from the VLBA maps. Similarly, the 5 GHz data are fitted with a single component with flux density 0.70 ± 0.07 mJy. Component S1 is not visible in the 1.6 GHz EVN map, although there are hints of a south-west extension in the map shown in Fig. 7 (bottom left). Additionally, the total flux density within the $5\sigma_{\text{rms}}$ contour at 1.6 GHz is higher than the peak flux by $\sim 20\%$ (see Tab. 2), further supporting the presence of extended flux in the EVN map. Therefore, A+S1 are likely unresolved into a single component (the EVN beam area is twice as large as the VLBA beam area). However, forcing a smaller beam to the EVN data and using a uniform weighting to improve the resolution results in a worse image sensitivity, which prevents us from fitting other components to the data in DIFMAP.

The simultaneous VLBA observations at the different frequencies (all performed on February 4, 2014) allow us to obtain a reliable measurement of the source spectral index. We measured the flux density of the core component (A) from maps obtained by matching the uv-range between the observing frequencies ($5 M\lambda - 50 M\lambda$), and we fitted a power-law to the flux densities at 1.6 GHz, 5 GHz, and 8.4 GHz. This returned a spectral index of $\alpha_A = 0.25 \pm 0.04$. Such rather flat value is consistent with the core spectral index on the kpc scale from LOFAR and JVLA data of 0.19 ± 0.02 (see §3.1). We also

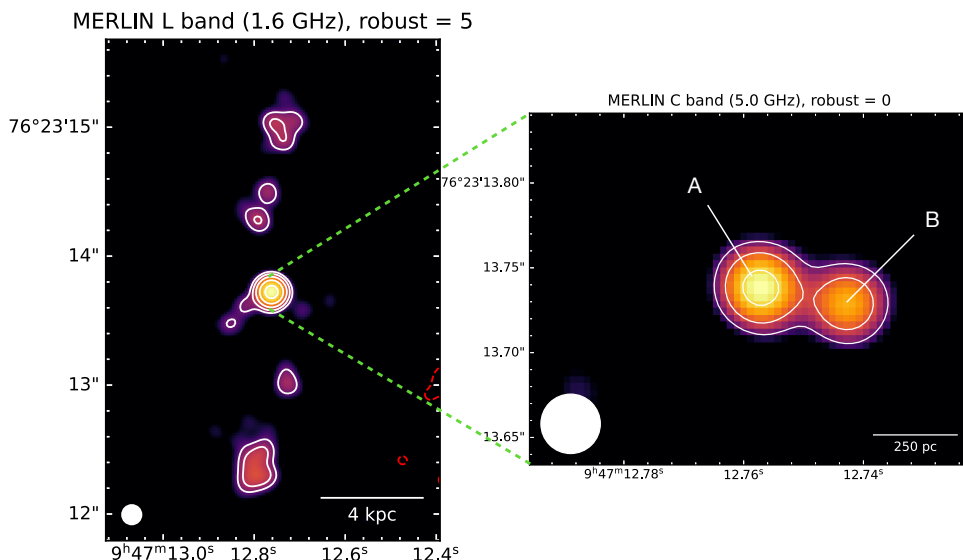


Fig. 6. e-Merlin images at 1.6 GHz (left) and 5 GHz (right) of RBS 797. In both panels, contours are drawn at $5\sigma_{\text{rms}}$, and increase by a factor of 2; the first negative contour (at $-5\sigma_{\text{rms}}$) is drawn in dashed red (not visible in the right panel). The beam is shown in the bottom left corner ($0.15'' \times 0.15''$ at 1.6 GHz and $0.035'' \times 0.035''$ at 5 GHz). See Tab. 2 for details on the resolution and noise level of the images. Structures discussed in this work are labelled.

Table 4. Results of model fit in DIFMAP applied to EVN and VLBA data of RBS 797.

(1)	(2)	(3)	(4)	(5)	(6)	(7)	(8)	(9)	(10)	(11)
Telescope	Project Code	Frequency [GHz]	Obs. Date	Robust	$\chi^2/D.o.f.$	Component	a [mas]	b/a	Φ [$^\circ$]	S [mJy]
VLBA	BG 224	1.6	Feb. 4, 2014	0	1.13 (229130)	A	2.5	1.0	0	0.75 ± 0.09
		5.0	Feb. 4, 2014	0	1.14 (54424)	A	5.8	0.7	-16.1	0.27 ± 0.04
		8.4	Feb. 4, 2014	0	1.19 (109548)	A	0.6	1.0	0	0.47 ± 0.05
	BE 056	5.0	Jul. 4, 2014	3	1.21 (13831)	A	0.05	1.0	0	0.40 ± 0.05
EVN	EG080	1.6	Feb. 26, 2014	0	1.16 (236740)	A	2.5	1.0	0	1.65 ± 0.17
		5.0	Mar. 9, 2014	0	1.07 (314572)	A	3.0	1.0	0	0.70 ± 0.07
	RSG05	5.0	May 3, 2013	0	1.12 (9068)	A	0.9	1.0	0	0.84 ± 0.09
	RSG07	1.6	Dec. 1, 2015	0	1.06 (12092)	A	3.4	1.0	0	1.91 ± 0.22

Notes. (1) Name of the radio telescope; (2) project code; (3) observing frequency; (4) date of the observations; (5) robust parameter used during imaging; (6) χ^2 /degrees of freedom; (7) label of the component; (8) major axis of the component, in mas; (9) ratio between minor and major axis of the component; (10) position angle of the ellipse describing the component, in degrees; (11) flux density of the component. See §2.1.1 for details.

deduce that the spectral index of component S1 is steeper than 0.65 at 3σ confidence, based on the sensitivity of the 5 GHz and 8.4 GHz observations (which do not detect this component).

Comparing our results with those presented in Gitti et al. (2013), we find the absence in our maps of the second component tentatively detected in the snapshot EVN observation at 5 GHz (performed on May 3, 2013) at a distance of 77 pc south-west from the radio core. The non-detection at all frequencies and between the different instruments suggests that it was, most likely, a spurious detection. A re-analysis of the data indicates that the component was in fact an artifact caused by the phase calibrator being resolved into a double itself.

Ultimately, we note that from the VLBA and EVN data we find no evidence of the second component B visible in the e-Merlin image at 5 GHz of Fig. 6. This supports our interpretation of B as extended radio emission, likely resolved out in the VLBI data due to the different uv-coverage.

3.4. Does the radio core of RBS 797 show time variability?

We note that there is an inconsistency in the flux density of RBS 797 between the different observations. At 1.6 GHz, the EVN total flux density is larger than the VLBA total flux density by a factor of ~ 1.75 , while at 5 GHz the EVN total flux density is larger than the VLBA total flux density by a factor of ~ 1.5 . This is inconsistent with the typical flux density scale error associated with the EVN and VLBA telescopes (around 10%).

To gain more insights on this difference, we retrieved other EVN and VLBA snapshot observations of RBS 797 (see §2.4 and Tab. 1) and we measured the (unresolved) flux densities in DIFMAP. Based on the flux densities reported in Tab. 4, we find that the 5 GHz emission oscillated between ~ 0.7 mJy and ~ 0.5 mJy between May 2013 and July 2014. The 1.6 GHz flux density increased from ~ 1 mJy to ~ 1.7 mJy between the 4th and the 26th of February 2014, and the following observation on December 1, 2015 measured a flux density of ~ 1.9 mJy (consistent with the previous measurement). A clear trend is that the EVN

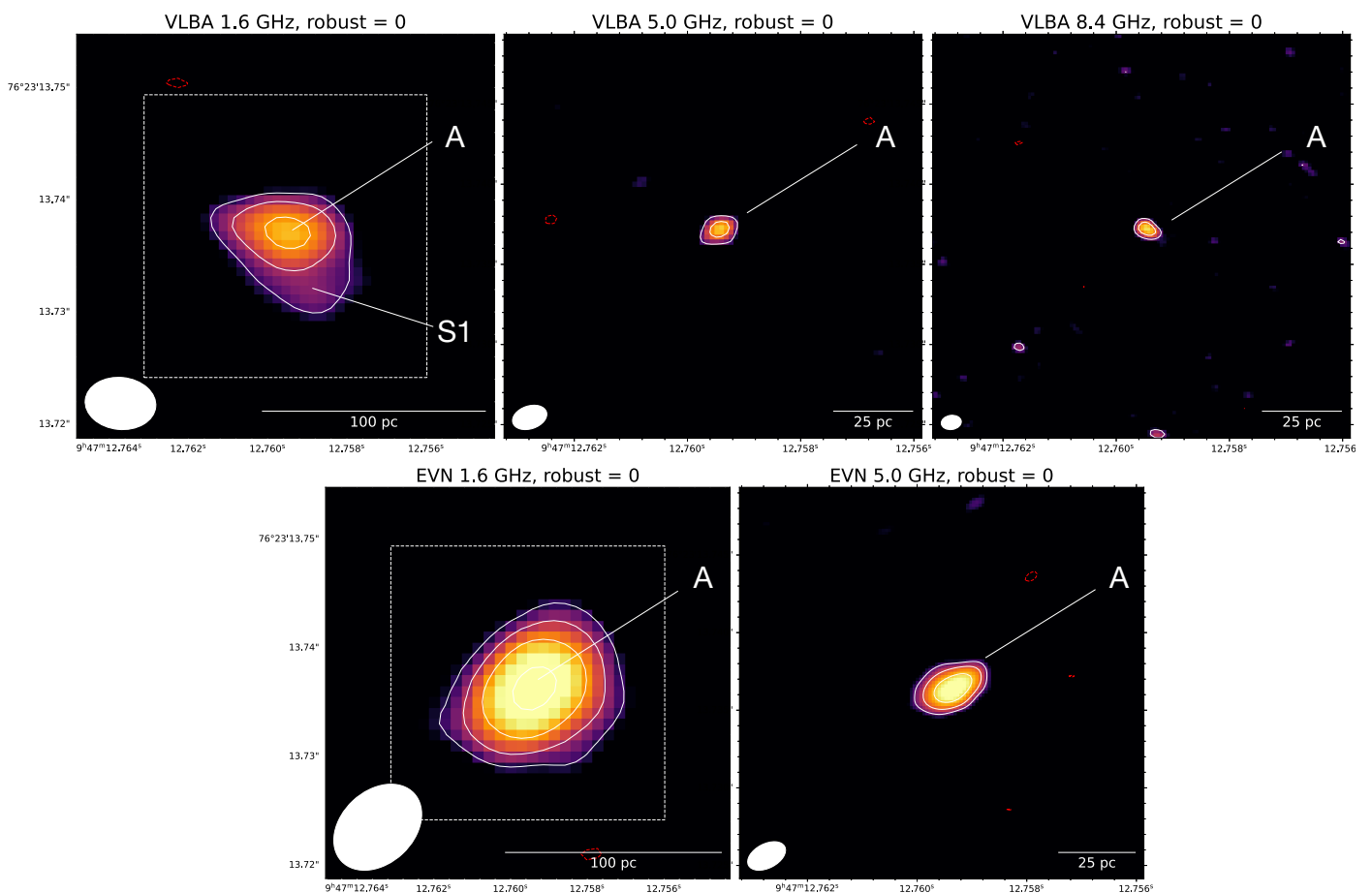


Fig. 7. VLBA and EVN maps of RBS 797 at different frequencies. *Top panels:* VLBA images at 1.6 GHz, 5 GHz, and 8.4 GHz. The beam sizes are 6.3×4.6 mas at 1.6 GHz, 2.2×1.4 mas at 5 GHz, and 1.3×0.9 mas at 8.4 GHz. *Bottom panels:* EVN images at 1.6 GHz and 5 GHz. The beam sizes are 9.1×6.7 mas at 1.6 GHz, and 2.6×1.6 mas at 5 GHz. In each panel, the beam is shown in the bottom left corner, and contours start at $5\sigma_{\text{rms}}$ and increase by a factor of 2; the first negative contour at $-3\sigma_{\text{rms}}$ is drawn in dashed red (see Tab. 2 for the resolution and noise levels of the images). The 1.6 GHz VLBA and EVN images have a matched field of view. The white dashed square shows the extent of the images at 5 GHz (EVN and VLBA) and at 8.4 GHz (VLBA). Structures discussed in this work are labelled.

flux densities are always higher than the corresponding VLBA flux densities at the same frequency. The 5 GHz EVN flux density (0.7 mJy) is also higher than the nearly contemporaneous 5 GHz eMerlin flux density (0.55 mJy). This may indicate a technical origin, or a different sensitivity to the structures of the source. However, we verified that matching the uv-coverage and image parameters does not solve such inconsistency. Excluding the Jodrell Bank and Westerbork stations from the EVN data (which provide the shortest spacings and therefore the highest sensitivity) still does not change these results. Additionally, the mismatch is not caused by transferring solution from a strongly variable phase calibrator (J0954+7435), which does not show significant flux density variations.

Interstellar scintillation may cause flux density variations in compact radio sources such as flat spectrum AGN, which typically occur on timescales of a few hours or days, at most (e.g., Koay et al. 2018). Yet, the variations measured in RBS 797 are on weeks and month timescales, and we do not find evidence of significant variability within the duration of each observation.

One possibility is that the variability is intrinsic to the source itself, which is not uncommon for the radio cores of BCGs (e.g., Hogan et al. 2015a,b). For active, long lived radio galaxies, the variation may be caused either by (a) a change in the accretion rate and thus in jet power and brightness; or (b) the launching of

distinct knots in the jets; or (c) if the jets are precessing, by the varying Doppler beaming of the ejected jet components. Considering the kpc-scale properties of the radio galaxy in RBS 797 (see §3.1 and §4.1.1), the above scenarios seem plausible. Alternatively, in the case of young radio sources with recently renewed jets, variability may be attributed to the synchrotron peak progressively shifting toward lower frequencies or to the jets interacting with the surrounding material (e.g., Bruni et al. 2019; Wołowska et al. 2021). If the radio core of RBS 797 is experiencing a fourth cycle of recently restarted AGN activity, then the above mechanism may provide a framework to interpret the possible variability.

Interestingly, we find evidence of time variability also on VLA scales. We compared the 4.8 GHz VLA observations published in Gitti et al. (2006) (performed in 2004) and our JVLA data at 5.5 GHz (4.5 – 6.5 GHz bandwidth), obtained in 2022. We built comparable maps by matching the uv-range, frequency, and bandwidth (4.8 GHz, 128 MHz) of the data. Using circles with radius of $1''$ centered on the radio core, we measured flux densities of $S_{4.8}^{2004} = 1.07 \pm 0.06$ mJy and $S_{4.8}^{2022} = 1.54 \pm 0.14$ mJy. The two measurements are different by a factor 1.44 at a significance of 2.9σ . Thus, we have independent indications of variability from the radio core of RBS 797, besides the evidence from VLBI data. Nevertheless, given the suspicious systematic

difference between the EVN and VLBA observations, and the poor sampling of the light curve, we cannot draw strong conclusions on the origin and amplitude of such variability, which currently remains unexplained. Future ad-hoc monitoring of this source may shed lights on this issue.

4. Discussion

4.1. Deciphering the morphology of the radio galaxy in RBS 797

The new radio images shown in the previous sections confirm the earlier claims that the central AGN of RBS 797 has been going through several episodes of activity, the directionality of which has changed over time. Combining our results with the previous works of Gitti et al. (2006, 2013); Ubertosi et al. (2021, 2023), we can summarize what is currently known on the outburst history of RBS 797 as follows. On 50 – 100 kpc scale the presence of three shock fronts and diffuse radio emission (see also Bonafede et al. 2023) supports an interaction between the AGN and its environment that dates back to ≈ 80 Myr ago. On scales of 10 – 50 kpc there are the perpendicular pairs of radio lobes and corresponding X-ray cavities that have similar ages (~ 30 Myr) down to a few Myr of accuracy (§3.1.3 and Tab. 3). Zooming into the inner 10 kpc, north-south curved jets are visible, with multiple sites of relativistic particle acceleration. The S-shaped jets are radiatively young, with an age of a few Myr (§3.1.2, §3.2, and Tab. 3). Ultimately, going down to hundreds and tens of pc an active core connected to a southward jet feature is visible, with possible evidence of time variability on months timescales (§3.3 & §3.4).

To understand the history of the multiple misaligned outbursts we need to identify the mechanism that drives such changes in orientation. A clear dynamical feature is the S-shaped jet morphology. These shapes have long been associated with precession over time of the jet axis (e.g., Rubinur et al. 2017; Horton et al. 2020; Nolting et al. 2023 and references therein), which is likely to be occurring in RBS 797. Indeed, we have independent evidence that the north – south jets are precessing. First, we noticed the presence of multiple hotspots in the radio maps, which is one of the expected signatures of precession (e.g., Mahatma et al. 2023). Second, the hotspots have similar spectral indices and radiative ages, indicating that particle are simultaneously being accelerated at each of these locations (see also Hardcastle et al. 2007), which can be a consequence of the swirling jet path (Horton et al. 2023). Considering the above information, in the next paragraphs we use the observed jet morphology in RBS 797 to constrain the main parameters of the precession motion.

4.1.1. Modelling jet precession

The distinct S-shape of the kpc-scale jets in RBS 797 visible in Fig. 2 may be explained with a precession motion around the jet axis. Such morphologies have been observed in several radio galaxies, from pc to hundreds of kpc scales (e.g., Liuzzo et al. 2009; Machalski et al. 2016; Bruni et al. 2021; Nandi et al. 2021). The morphological signatures of jet precession can be linked to the dynamical parameters that regulate such motion. These are, mainly, the precession period P , the half-opening angle of the jet precession cone ψ , the inclination of the jet along the line of sight i , and the jet advance speed v . The exact mapping between the radio morphology and these quantities depends

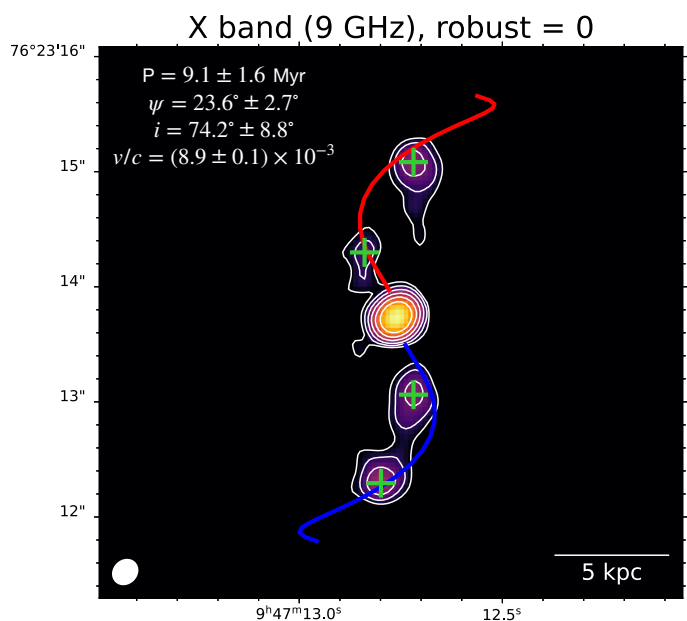


Fig. 8. Jet precession in RBS 797. Precession model of Hjellming & Johnston (1981) fitted to the radio images of the kpc-scale jets in RBS 797. Contours are the same as those shown in Fig. 2. The red line represents the receding jet path and the blue line represents the approaching jet path. The location of the green crosses corresponds to the position of the observed hotspots, while their extent represents the resolution of the radio observation (the beam is shown in the bottom left corner) Best fit parameters are reported in the top left corner. We note that the uncertainties on the best fit parameters represent the combination of statistical and systematic uncertainties (see §4.1.1 for details).

on the model assumed for the physics of jet propagation and precession.

Here we consider the kinematic precession model of Hjellming & Johnston (1981), which includes relativistic effects⁴. The model parameters are the distance to the source (d), the position angle of the jet precession axis in the plane of the sky (χ), the precession period (P), the half-opening angle of the jet precession cone (ψ), the precession axis inclination to the line of sight (i), and the jet advance speed (v/c). From the equations detailed in Hjellming & Johnston (1981), the model predicts the position at a time $t_{eject} + \Delta t$ of two opposite jet blobs launched from the SMBH at a time t_{eject} . The position is expressed in the form of offsets from the core position δRA and δDEC . Evolving the model from the initial time t_{eject} (for example, 20 Myr ago) to t_{obs} (i.e. the present time) produces the predicted model jet path projected onto the plane of the sky over 20 Myr of jet activity. Such model can be readily compared to the real jet path observed from radio maps.

In order to derive the parameters of the jet precession motion in RBS 797, we followed a similar approach to that of Coriat et al. (2019). We used the `scipy.optimize` package to minimize the difference between (a) the observed offsets of each hotspot (H1, H2, H3 and H4) with respect to the core, δRA_{obs} and δDEC_{obs} , and (b) the jet path predicted by the model in the form δRA_{mod} and δDEC_{mod} . The observed hotspot offsets have

⁴ While it was built to fit the jet morphology of the microquasar SS433, it does not assume any a-priori condition related to microquasars, and it is relatively simple. Thus, it can be generalized to describe jets from radio galaxies. Indeed, it has been used before to model extragalactic AGN jets (see e.g., Rubinur et al. 2017; Kharb et al. 2019)

been weighted by the area of the radio beam during the minimization process.

The model parameters that we fixed before evolving the model are the distance to the source $d = 1881.7$ Mpc (the luminosity distance), and the position angle of the jet precession axis in the plane of the sky, $\chi = 90^\circ$ (that is the position angle of the whole S-shaped jet structure, measured from the west axis). We set constraints in input to the model parameters as follows:

- P : the precession period was bound to vary between 2 Myr (the lowest radiative age we measure from the spectral modelling of the jets, see Fig. 4, *right panel*) and 20 Myr (twice the maximum radiative age we measured). We verified that for $P > 20$ Myr the model predicts a jet bending on scales of tens of kpc, which would be in disagreement with the observed bending on a few kpc scale.
- ψ : the half-opening angle of the jet precession cone was bound to vary between 10° and 30° to approximately match the observed morphology of the S-shaped jets.
- i : the jet precession axis inclination with respect to the line of sight was bound between 60° and 90° . As noted in §3.1, the symmetry of the jets suggests that the whole structure is not strongly oriented towards the observer.
- v/c : the jet advance speed in units of the speed of light c was bound between $10^{-3}c$ and $10^{-1}c$, in comparison with typical speed of kpc – scale jets (e.g., Meyer et al. 2017; Kappes et al. 2019; Perucho et al. 2019).

The minimization procedure consists in `scipy.optimize` exploring the parameter space of the above quantities and computing every time the predicted jet path. The optimized model is the one for which the distance between the predicted and observed jet paths is the smallest. The minimization was realized 1000 times, and we assumed the dispersion of the derived parameters around the mean as a good estimate of the statistical error σ_{stat} . Additionally, the minimization was performed not only at one frequency, but using all the available radio maps that detect the hotspots: LOFAR at 144 MHz, JVLA at 3 GHz, 5.5 GHz, 9 GHz (Fig. 2), and e-Merlin at 1.4 GHz (Fig. 6). The dispersion around the mean of the precession parameters at different frequencies was assumed as a good indicator of the systematic error σ_{syst} . The final uncertainty on each best fit parameter is given by $\sqrt{\sigma_{stat}^2 + \sigma_{syst}^2}$.

We show in Fig. 8 an overlay of the best-fit precession model on the 9 GHz JVLA image of RBS 797, where we also report the best-fit parameters. The predicted jet path is color coded according to the approaching (blue) and the receding (red) jet. We obtain a precession model with period $P \sim 9$ Myr, rotating with a half-opening precession cone angle of $\psi \sim 24^\circ$ and inclined by $i \sim 74^\circ$ degrees with respect to the line of sight. The jet advances with a speed of $v \sim 10^{-2}c$. We observe that within the uncertainties on the hotspots position (given by the resolution of radio observations), the model provides a nice representation of the jets morphology. The predicted inclination along the line of sight is in line with the jets mainly lying in the plane of the sky. The best-fit jet advance speed agrees with the order-of-magnitude dynamical speed of the jets: based on the radiative age of the jet structures ($\sim 2 - 7$ Myr) and the jet length of ~ 8 kpc, we would expect a dynamical velocity ranging between $0.004c \lesssim v_{dyn} \lesssim 0.01c$. We additionally note that the comparison between the estimated jet radiative ages (§3.1.2) and the predicted precession period indicates that the jets are currently half way through a full precession round.

4.1.2. The connection between the inner jets and the outer lobes: single or multiple precession modes?

The precession model detailed above provides a good description of the north – south jet motion. However, it is not straightforward to fit the older outbursts into this scenario. The perpendicular pairs of radio lobes on ~ 50 kpc scales have been inflated over similar timescales, and do not lie on the jet path predicted by the precession model (see Fig. 8). Here we discuss whether the morphological evidence support a single dynamical effect, or if the combination of multiple mechanisms is required to explain all the outbursts.

Can a single precession mode explain the multi-faceted morphology visible in Fig. 2? Numerical simulations found that a prolonged wobbling outflow coupled with jet self-interactions can cause very complex morphologies to appear (e.g., Horton et al. 2020, 2023; Lalakos et al. 2022; Nolting et al. 2023). Synthetic radio maps presented in these works show a plethora of structures in multiple directions (even orthogonal ones). Nolting et al. (2023) stressed that the viewing angle of the observer (i in this work, θ in their work) may generate very different apparent radio shapes. The case of RBS 797 may be akin to those of the above simulations. However, the most “misaligned morphologies” (as those observed in RBS 797) occur either when the half-opening angle of the precession cone is large (up to $\sim 45^\circ$) or when the precession axis is nearly aligned with the line of sight ($i \leq 45^\circ$). On the contrary, we found in §4.1.1 that the precession cone is relatively narrow ($\psi \sim 24^\circ$) and that the source is not strongly oriented towards us ($i \sim 74^\circ$). Thus, the above scenarios may apply to RBS 797 only if the parameters that regulate the precession motion are time dependent (e.g., Martí et al. 1997; Laing & Bridle 2014; Giri et al. 2022). For example, if the half-opening angle of the precession cone ψ was larger in the past, and possibly as high as 45° , then it would be possible to find radio emission in the direction perpendicular to that of the current jet axis. Thus, we argue that a simple and stationary precession model cannot explain the whole history of AGN activity.

We can only be speculative about mechanisms that are more elaborate than a single precession mode. A first possibility is that precession was already in place ~ 30 Myr ago, during the large lobe formation. A short precession period (a few Myr) and a large precession cone half-opening angle ($\psi \approx 45^\circ$) would explain how the N – S and E – W lobes (and the associated cavities) have very similar radiative and dynamical ages (see also Ubertosi et al. 2021). The end of the activity around 20 Myr ago (see §3.1.3) could have been followed by a jet axis flip by a large angle (nearly 90°). As a consequence, the following (and present) jet activity, started within the last ~ 10 Myr, is oriented in a different direction.

A second idea involves the superposition of two wobbling modes. Besides precession, the nutation motion of jets has also been predicted in the context of jet dynamics (Gangardt et al. 2021) and observationally confirmed on pc scales (Britzen et al. 2018; Dominik et al. 2021; von Fellenberg et al. 2023). We can hypothesize that the jets in RBS 797 experience a long period nutation of the jet axis modulated by a shorter time precession motion. A long period nutation (a few tens of Myr) with a wide nutation angle would explain how the large E-W lobes are orthogonal to the current N-S jets, and a small period precession (a few Myr) would account for the nearly coeval lobes on 50 kpc scales and the S-shaped jets on 10 kpc scales.

Interestingly, all the above processes are usually associated with the presence of binary SMBHs in the central engine (e.g., Merritt & Ekers 2002; Britzen et al. 2018). Below we discuss how the spectral properties of the radio plasma can provide further insights.

4.1.3. The connection between the inner jets and the outer lobes: injection index and jet power

The injection index of the radio plasma has changed between the previous activity that produced the large E-W and N-S radio lobes ($\Gamma \sim 0.54$, see §3.1.3 and Tab. 3) and the current activity of the north – south jets ($\Gamma \sim 0.9$, see §3.1.2). This indicates that the initial energy distribution of the electrons powering the current north – south jets was characterized by a relatively higher number of particles at low energies. We noted in §3.1.2 that the steep injection index of the jets is consistent with those found in powerful FR IIs. Conversely, the injection index of the radio lobes is consistent with the range of $0.5 \leq \Gamma \leq 0.7$ expected for radio galaxies (including FR Is, e.g., Laing & Bridle 2013). It has been argued that the injection index positively scales with the jet mechanical power (Blundell et al. 1999; Konar & Hardcastle 2013). This scaling would agree with powerful FR IIs having steeper injection indices. Interestingly, Konar & Hardcastle (2013) also reported that, in sources that show multiple episodes of activity, a difference in the injection index is expected if the jets change their direction from one outburst to the other.

These arguments are particularly relevant in the case of RBS 797. Specifically, the steeper Γ of the youngest AGN activity supports a recent transition from an FR I radio galaxy (the older, large lobe phase on 50 kpc scales that carved out the E-W and N-S cavities) to a more powerful FR II (the current north – south twisted jets on ~ 5 -10 kpc scales). The morphology of the radio emission is also in agreement with this interpretation (see Fig. 2): the diffuse morphology of the large radio lobes and the presence of hotspots in the north – south jets favours a FR I interpretation of the former activity and a FR II interpretation of the latter (Fanaroff & Riley 1974).

This transition may have been driven by a mechanism that could either be extrinsic or intrinsic to the central engine. In the first case, a change in the accretion rate of the SMBH may have determined an increase of the mechanical power. RBS 797 is a strongly cooling galaxy cluster, and the rate at which gas cools out of the ICM and ultimately feeds the AGN is expected to flicker over time (e.g., Gaspari et al. 2012; Li et al. 2015). In the second scenario, the conditions of the central engine may have changed between the outbursts. It has been previously claimed that RBS 797 may host (or may have hosted in the past) binary SMBH (Gitti et al. 2006, 2013; Ubertosi et al. 2021). If the binary SMBHs merged between the older and the younger outbursts, this may have caused a flip of the new SMBH spin (Merritt & Ekers 2002), which would explain the different direction of the new jet activity. The sudden increase in black hole mass may also be linked to higher – power jets (Blandford & Znajek 1977). Alternatively, the older and younger outbursts may not have been driven by the same SMBH: if the binary has not coalesced, it is possible that after one SMBH switched off (the one producing the lobe emission) the second SMBH turned on in a different direction. If so, it would be unsurprising to observe different jet powers in successive outbursts.

4.1.4. Alternative scenarios for the outer lobes and inner jets

An alternative mechanism that has been invoked to explain secondary lobes of radio galaxies, misaligned from the main jets, is that of backflows. We thus considered the hypothesis that the N-S cavities and corresponding radio lobes resulted from a backflow of the jets in the east-west direction. However, this model is unlikely to be applicable to RBS 797, given the evidence listed as follows. (1) Backflow formation: plasma from FR II-type jets can be backflowed towards the core owing to pressure imbalance with the surrounding thermal medium. If the environment is highly asymmetric, the backflowed plasma can be diverted towards the direction of the minimum pressure path, usually the minor axis of the host galaxy (e.g., Leahy & Williams 1984; Capetti et al. 2002; Saripalli & Subrahmanyan 2009). In RBS 797, the E-W lobes are already aligned with the minor axis of the host galaxy (see the optical images in Cavagnolo et al. 2011), and thus it is unlikely that the backflow could traverse the major axis and excavate cavities by displacing the hot gas, as in that direction the gas is much denser. (2) Spectral index and plasma age: backflows typically exhibit steeper spectral indices and longer radiative ages compared to the plasma of the main lobes due to their greater distance from the site of the most recent particle acceleration (e.g., McKean et al. 2016; Cotton et al. 2020; Morganti et al. 2021; Brienza et al. 2020, 2023). In this respect, the similar age and spectral index of the perpendicular lobes in RBS 797 argue against a backflow model. (3) Radio galaxy classification: backflows are generally associated with FR II radio sources, where they represent plasma escaping the hotspots and returning towards the galaxy (e.g., Leahy & Williams 1984; Hodges-Kluck & Reynolds 2011; Whitehead & Matthews 2023). However, the AGN activity responsible for inflating the east-west radio lobes in RBS797 is classified as FR I based on radio power and morphology (this work; Gitti et al. 2006).

For the north-south jets on kpc scales, we consider the alternative hypothesis that the jets are bent due to the interaction with the surrounding gas. In this scenario, the four compact bright regions (Fig. 2c) are not hotspots but rather jet knots. However, we find that this is unlikely the case for the jets in RBS 797. High-power jets from BCGs in cool core clusters are hardly bent by the hot and rarified ICM during their earliest stages of propagation (at distances $\lesssim 10$ kpc; e.g., Bourne & Yang 2023). On the contrary, such jets typically push aside the hot gas, which has low electron densities, and create cavities. In RBS 797, the ICM density within 10 kpc from the center is $\sim 0.1 \text{ cm}^{-3}$ (Ubertosi et al. 2023). This value is typical of strong cool-core clusters (e.g., Sanderson et al. 2009) and is insufficient to disrupt the jets. While cooler and denser gas phases might in general be more effective in bending a jet, we may likely rule out this possibility as well based on the findings of Cavagnolo et al. (2011) and Calzadilla et al. (2022) for RBS 797. The BCG of RBS 797 hosts a filamentary nebula of warm gas, a common feature in cool core clusters, which coincides with the region of most efficient cooling in the ICM (Ubertosi et al. 2023). The nebula is highly asymmetric, being structured in filaments that extend for about 20 kpc only in the south direction. The filaments are spatially correlated with the southern jet (Cavagnolo et al. 2011), but this is more likely explained in the context of jet-induced cooling: jets can induce local instabilities in the ICM, which cools to lower temperatures and produces co-spatial filamentary structures (e.g., McNamara et al. 2016). Thus, we find very unlikely that a dense environment may cause a bending of the jets in RBS 797. In general, and possibly most importantly, we highlight that the observed high degree of symmetry between the north and

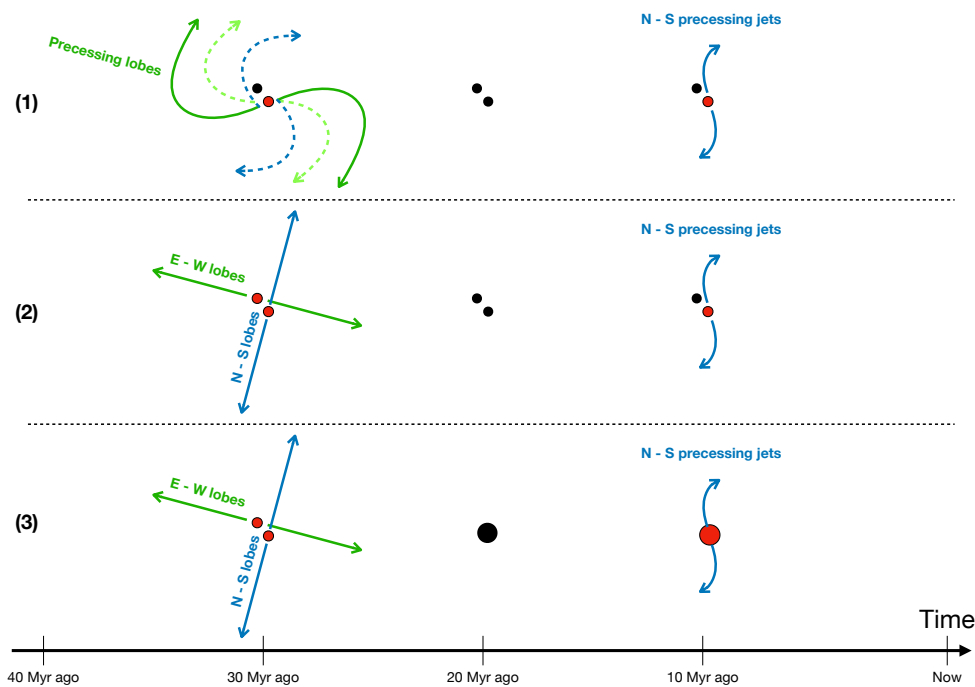


Fig. 9. Schematic representation of the three scenarios involving binary SMBHs at the center of the radio galaxy in RBS 797. See §4.2 for details. Arrows represent jets, while circles represent SMBHs (red indicates an active one, black indicates a quiescent one). Blue lines represent the jet activity in the N-S direction, while green lines represent the jet activity in the E-W direction. The dashed lines in panel 1 reflect the precession of the radio lobes on ~ 50 kpc scales.

south jets (in terms of shape, radio brightness, and radio spectral properties) is difficult to reconcile with an external environmental influence, as the environment itself exhibits clear asymmetry.

Ultimately, we caution that the definitions of knots and hotspots are ambiguous. Usually, what separates the two is their location within the radio galaxy: knots are defined as loci along the jet path where the jet encounters material and the plasma is accelerated, whereas hotspots are termination points of the jet flow (e.g., Hardcastle et al. 2007). However, numerous observations challenge such simple strategy. For instance, the existence of multiple bright compact features associated with the jet termination indicates that jets do not always terminate at a single location (Hardcastle 2008). Previous works studying precessing jets labelled as “hotspots” the compact features found along the twisting jet path (e.g., Cox et al. 1991; Hardcastle et al. 2007; Krause et al. 2019; Horton et al. 2020, 2023), because in precessing jets the termination point of the ejected plasma changes with time, due to the different launching angle. Given these arguments and considering that jet precession most likely explains the observed properties of the jets in RBS 797, we opted for the term “hotspots” in this work.

4.2. Is the central AGN powered by binary SMBHs?

Over time, the AGN activity in RBS 797 has been characterized by different processes, including a clear jet precession and possibly a reorientation event between the older and the most recent outbursts. Leveraging the morphological and spectral information on this radio galaxy, we found strong independent evidence for claiming the existence of binary SMBHs in the core of RBS 797. These include:

- The clear twisted morphology of the jets on kpc scale and the existence of multiple, coeval hotspots along these structures. These features are strongly indicative of a precession motion, which in turn is usually attributed to the presence of massive binary SMBHs orbiting each other (e.g., Nandi et al. 2021; Horton et al. 2023).

- The existence of the perpendicular and equidistant E – W and N – S lobes (and corresponding X-ray cavities) on larger scales (~ 50 kpc). The dynamical estimates (from X-ray data, Ubertosi et al. 2021) and the radiative estimates (this work, §3.1.3) nicely agree on the fact that both pairs of lobes/cavities were formed around 30 Myr ago and are coeval (with a ~ 10 Myr uncertainty). The analysis of the radio spectrum further revealed that the jet activities that powered these outbursts had a very similar duration of the active phase (~ 10 Myr) and of the fading phase (~ 20 Myr).

Additionally, the putative variability of the radio core would be expected from binary SMBHs models (e.g., Kun et al. 2014; Komossa et al. 2023; Gutiérrez et al. 2023). However, given the unconfirmed nature of such variability we do not further address this topic.

We are aware that interactions between a single SMBH and its accretion disc can also induce jet precession (Bardeen & Petterson 1975), due to a forced alignment of the SMBH spin and the disk spin. The precession rate is expected to be slow, and the change in the jet orientation is a single event. This model would be hard to apply to RBS 797: not only we have evidence for multiple changes in jet orientation over time (see also Ubertosi et al. 2021, 2023), but most importantly the Baarden - Petterson effect would not be able to account for the perpendicular, equidistant and coeval outer lobes (see also Krause et al. 2019 for similar arguments).

Therefore, in the following we assume that the presence of binary SMBHs in RBS 797 is the most likely explanation for the morphological and spectral radio properties. Based on this assumption, we can envisage three possible scenarios to explain the outburst history of the central radio galaxy. These are presented below (see also the schematic view of Fig. 9):

1. *Binary SMBHs with one of them active and an evolving precession (Fig. 9, panel 1).* If precession was already in place 30 Myr ago with a wide opening angle ($\geq 45^\circ$, to explain the perpendicular position of the outer lobes) and a small precession period (< 10 Myr, to explain the similar age of the

structures), then the formation of a multi-lobed morphology on tens of kpc scales would be expected (Nolting et al. 2023; Horton et al. 2023). Following this scenario (upper row in Fig. 9), after a period of inactivity one of the SMBH in the binary system started again its activity in the N – S direction (producing the N-S twisted jets on ~ 10 kpc scales, see Fig. 2), with the gravitational perturbation of the secondary component still causing the jets to precess. Assuming that a single jet episode created both the N – S and E – W outer lobes would be consistent with the very similar injection spectral index $\Gamma \sim 0.54$ of the perpendicular structures on 50 kpc scales (see §4.1.3). The change in jet precession axis from the older (on 50 kpc scales) to the younger (on 10 kpc scales) activity may have been induced either by a sudden change of the SMBH spin axis, or by a long-term nutation motion of the jet direction (see §4.1.2).

2. *Binary SMBHs, both of them active 30 Myr ago and only one active now (Fig. 9, panel 2).* Another possibility to explain the coeval origin of the perpendicular outer lobes is to hypothesize that both SMBHs were active ~ 30 Myr ago (middle row in Fig. 9; see also Ubertosi et al. 2021). This scenario would not require jet reorientation to occur between the older and the younger outbursts: one of the SMBHs would simply renew its jets in the N – S direction, and the other would remain silent.
3. *Binary SMBHs, both of them active 30 Myr ago, then a merger around 10 Myr ago and the resulting single SMBH active now (Fig. 9, panel 3).* This case assumes a coeval activity around 30 Myr ago of both SMBHs (as the second scenario), but includes the coalescence of the two SMBHs into a single SMBH of higher mass in between the older and younger outbursts (last row in Fig. 9). On the one hand, it would be quite unlikely to serendipitously catch a post-merger SMBH that went through AGN activity before and after the event. On the other hand, this scenario would also explain (contrarily to the first two) other results that we presented. A merger between SMBHs is the key mechanism behind the spin-flip of the central engine (Merritt & Ekers 2002), that is the sudden and large change in jet pointing direction (as observed in RBS 797 between the older and younger outbursts). Additionally, a change in the intrinsic properties of the AGN (in this case, the increased SMBH mass) would be compatible with the observed change of synchrotron injection index (Konar & Hardcastle 2013) and the likely increase of the jet power (Blandford & Znajek 1977), as we discussed in §4.1.3.

The above scenarios are all based on indirect evidences of binary SMBHs in RBS 797.

Do we have direct evidence for the presence of two compact radio cores in the available data? The VLBI observations presented in §3.3 clearly detect a single, compact component at the center of the radio galaxy. If there was a second SMBH on tens of pc scales, it may be undetected owing to a low level of activity. Based on the sensitivity at 1.4 GHz of the VLBA data, we estimate a 3σ upper limit on the radio power of any radio-compact component on tens of pc scales of $P_{1.4\text{GHz}} \leq 3 \times 10^{22}$ W/Hz.

Therefore, we tend to exclude that a secondary SMBH is present above tens of pc scales. In this context, it is interesting to note that the precession period caused by the geodetic perturbation of the SMBH spin can be linked to the binary separation. Following Krause et al. (2019); Horton et al. (2020) we can place an upper limit on the binary separation with the following

expression:

$$d_{pc} < 0.18 P_{Myr}^{2/5} M_9^{3/5} \quad (5)$$

where d_{pc} is the binary separation in parsec, P_{Myr} is the precession period in Myr and M_9 is the active black hole mass in units of $10^9 M_\odot$. The assumptions behind the above equation are that the binary SMBHs are orbiting each other in a circular orbit, and that the observed precessing jets are launched by the more massive black hole. We measured in §4.1.1 a precession period of $P = 9.1 \pm 1.6$ Myr. The mass of the SMBH in RBS 797 has been estimated to be around $1.5 \times 10^9 M_\odot$ (Cavagnolo et al. 2010; Ubertosi et al. 2023). We obtain an upper limit on any binary separation of $d_{pc} < 0.6$ pc. This is an order of magnitude smaller than the highest resolution that can be achieved with the available VLBI data (5 pc ~ 1 mas in the 8.4 GHz VLBA observations). Therefore, the VLBI data do not contradict the binary interpretation.

Overall, even if both SMBHs were active (i.e. potentially visible through their radio emission), they would be hard to resolve at the redshift of RBS 797 ($z = 0.354$). An alternative method to investigate this point would be to search for double-peaked broad and narrow optical lines (e.g., [OIII]) in the core of the BCG, potentially caused by the orbiting binary (see e.g., Smith et al. 2010). At present, the existing optical spectral data of the BCG in RBS 797 (Fischer et al. 1998) are not suited for this type of analysis, and follow-up observations are vital.

5. Summary and Conclusions

The multi-scale and multi-frequency radio data presented in this work represent a crucial complement to the deep *Chandra* data presented by Ubertosi et al. (2021, 2023). While the X-ray observations gave clear insights into the *footprints* of feedback on the ICM, the radio observations revealed the direct details of jet evolution in the cluster RBS 797. Here we summarize our results.

1. The LOFAR (144 MHz, with international stations) and JVLA (3 GHz, 5.5 GHz, 9 GHz) data allowed us to unveil the morphological and spectral properties of the radio galaxy between 10 – 50 kpc (the scale of the perpendicular pairs of radio lobes) and between 2 – 10 kpc (the scale of the inner jets). We present the first images of the large scale lobes at sub-arcsecond resolution at 144 MHz (0.3'' resolution) and 3 GHz (0.9'' resolution). These images confirm the co-spatiality of the radio lobes with the perpendicular X-ray cavities. By fitting a CI-off model to the observed spectra, we find that the radiative age of the E-W lobes (31.4 ± 6.6 Myr) and of the N-S lobes (32.1 ± 9.9 Myr) supports a coeval origin of the perpendicular outbursts, that also have similar *active phase* duration (~ 12 Myr) and *passive phase* duration (~ 19 Myr). These ages are in good agreement with the X-ray estimates of the cavities and shock ages. Based on the 144 MHz – 9 GHz emission from the inner N-S jets (on scales of ≤ 10 kpc), we (a) confirm the S-shaped jet morphology; (b) show the presence of two hotspots per jet with a similar radiative age; (c) estimate the age of the twisting N-S jets to be less than ~ 8 Myr. Based on these results, we determine that jet precession (with period ~ 9 Myr and jet advance speed $\sim 0.01c$) can explain the morphological and spectral properties of the N-S twisted jets. We also find that the injection index of the synchrotron emission has steepened between the large scale, older outburst ($\Gamma \sim 0.5$) and

- the younger S-shaped jets ($\Gamma \sim 0.9$). This evolution in injection index may suggest that the central radio galaxy has transitioned from an FR I-like activity to an FR II-like one around ~ 10 Myr ago, when the N-S jet activity started.
2. The e-Merlin observations at 1.6 GHz show the precessing N-S jets at the highest resolution currently available ($0.15''$). With the e-Merlin 5 GHz observations ($0.035''$ resolution), the core emission is resolved into two components (separated by 250 pc), that we interpret as the radio core (component A, $S = 0.55 \pm 0.04$ mJy) and diffuse, remnant emission from the previous outbursts (component B, $S = 0.38 \pm 0.04$ mJy).
 3. The EVN data at 1.6 GHz and 5 GHz reveal the presence of a single, compact core at the heart of RBS 797 (component A). The VLBA data are in agreement with the EVN detection of a single component, but we also find evidence in the 1.6 GHz VLBA data of a faint jet-like feature headed south (component S1, $S = 0.27 \pm 0.04$ mJy at 1.6 GHz). We also show that there is evidence for monthly-scale time variability of the core radio emission. There is a suspicious (but possibly serendipitous) systematic flux density difference between the EVN and VLBA observations, which may indicate that the variability is not physical. However, we find that the flux measured with the VLA between 2004 and 2022 has also varied (with a significance of 2.9σ). Future ad-hoc monitoring is required to confirm the radio core variability.
 4. Piecing together these results, we discussed that a backflow scenario is not supported, whereas we argued that RBS 797 likely hosts (or hosted) binary active SMBHs in the past. The idea of binary black holes is in agreement with (a) the coeval origin of the large, perpendicular radio lobes (and corresponding X-ray cavities); (b) the very similar active and inactive phase duration of the perpendicular radio lobes; (c) the clear jet precession of the N-S jets; (d) the sudden transition in energy budget, jet power, and synchrotron injection index between the successive outbursts. Radio variability (if confirmed) would be an additional clue. We stress that the detection of a single component in the VLBI data is still consistent with the binary black hole interpretation: the predicted separation of the binary SMBHs (0.6 pc) is an order of magnitude smaller than the resolution of the available radio data (5 pc).

Our study highlights how a multi-frequency approach can help to discriminate between different scenarios. It also underlines the critical need for high resolution observations that are also sensitive to large scale, diffuse radio emission (such as the LOFAR data with international stations, or the 3 GHz JVLA data). This is required to connect the fine structure of the jets in radio galaxies with the complex geometry of their large expanding lobes.

This work adds up to the handful comparisons between radiative ages and X-ray dynamical timescales of radio lobes and corresponding X-ray cavities (see Biava et al. 2021 and Kolokythas et al. 2020). Interestingly, in the case of RBS 797 the radio lobes, the X-ray cavities, and the associated weak shock front have consistent ages down to only a few Myr of uncertainties, thus being a critical test for the AGN – ICM connection.

Acknowledgements. The authors thank the referee for their clear suggestions, which improved the scientific quality of this manuscript. F. Ubertosi thanks F. Brighenti for the insightful discussions. e-MERLIN is a National Facility operated by the University of Manchester at Jodrell Bank Observatory on behalf of STFC. The European VLBI Network is a joint facility of independent European, African, Asian, and North American radio astronomy institutes. Scientific results from data presented in this publication are derived from the following EVN project code(s): EG080A, EG080B, RSG05, RSG07. The National Radio Astronomy Observatory is a facility of the National Science Foundation operated under cooperative agreement by Associated Universities, Inc. This paper is based

(in part) on data obtained with the International LOFAR Telescope (ILT) under project code LC10_010. LOFAR (van Haarlem et al. 2013) is the Low Frequency Array designed and constructed by ASTRON. It has observing, data processing, and data storage facilities in several countries, that are owned by various parties (each with their own funding sources), and that are collectively operated by the ILT foundation under a joint scientific policy. The ILT resources have benefitted from the following recent major funding sources: CNRS-INSU, Observatoire de Paris and Université d'Orléans, France; BMBF, MIWF-NRW, MPG, Germany; Science Foundation Ireland (SFI), Department of Business, Enterprise and Innovation (DBEI), Ireland; NWO, The Netherlands; The Science and Technology Facilities Council, UK; Ministry of Science and Higher Education, Poland[7]. EDR is supported by the Fondazione ICSC, Spoke 3 Astrophysics and Cosmos Observations. National Recovery and Resilience Plan (Piano Nazionale di Ripresa e Resilienza, PNRR) Project ID CN_0000013 "Italian Research Center for High-Performance Computing, Big Data and Quantum Computing" funded by MUR Missione 4 Componente 2 Investimento 1.4: Potenziamento strutture di ricerca e creazione di "campioni nazionali di R&S (M4C2-19)" - Next Generation EU (NGEU). MB acknowledges support from INAF under the Large Grant 2022 funding scheme (project "MeerKAT and LOFAR Team up: a Unique Radio Window on Galaxy/AGN co-Evolution"). AB acknowledges support from the ERC Stg DRANOEL n. 714245. AI acknowledges funding from the European Research Council (ERC) under the European Union's Horizon 2020 research and innovation programme (grant agreement No. 833824).

References

- Argo, M. 2015, arXiv e-prints, arXiv:1502.04936
- Bardeen, J. M. & Petterson, J. A. 1975, *ApJ*, 195, L65
- Begelman, M. C., Blandford, R. D., & Rees, M. J. 1980, *Nature*, 287, 307
- Bertocco, S., Goz, D., Tornatore, L., et al. 2020, in *Astronomical Society of the Pacific Conference Series*, Vol. 527, *Astronomical Data Analysis Software and Systems XXIX*, ed. R. Pizzo, E. R. Deul, J. D. Mol, J. de Plaa, & H. Verkoeter, 303
- Biava, N., Brienza, M., Bonafede, A., et al. 2021, *A&A*, 650, A170
- Birzan, L., McNamara, B. R., Nulsen, P. E. J., Carilli, C. L., & Wise, M. W. 2008, *ApJ*, 686, 859
- Blandford, R. D. & Znajek, R. L. 1977, *MNRAS*, 179, 433
- Blundell, K. M., Rawlings, S., & Willott, C. J. 1999, *AJ*, 117, 677
- Bonafede, A., Gitti, M., La Bella, N., et al. 2023, *A&A*, 680, A5
- Bourne, M. A. & Yang, H.-Y. K. 2023, *Galaxies*, 11, 73
- Brienza, M., Gilli, R., Prandoni, I., et al. 2023, *A&A*, 672, A179
- Brienza, M., Morganti, R., Harwood, J., et al. 2020, *A&A*, 638, A29
- Britzen, S., Fendt, C., Witzel, G., et al. 2018, *MNRAS*, 478, 3199
- Bruni, G., Brienza, M., Panessa, F., et al. 2021, *MNRAS*, 503, 4681
- Bruni, G., Panessa, F., Bassani, L., et al. 2019, *ApJ*, 875, 88
- Bruno, L., Gitti, M., Zanichelli, A., & Gregorini, L. 2019, *Astronomy & Astrophysics*, 631, A173
- Calzadilla, M. S., McDonald, M., Donahue, M., et al. 2022, *ApJ*, 940, 140
- Capetti, A., Zamfir, S., Rossi, P., et al. 2002, *A&A*, 394, 39
- Carilli, C. L., Perley, R. A., Dreher, J. W., & Leahy, J. P. 1991, *ApJ*, 383, 554
- CASA Team, Bean, B., Bhatnagar, S., et al. 2022, *PASP*, 134, 114501
- Cavagnolo, K. W., McNamara, B. R., Nulsen, P. E. J., et al. 2010, *ApJ*, 720, 1066
- Cavagnolo, K. W., McNamara, B. R., Wise, M. W., et al. 2011, *ApJ*, 732, 71
- Coriat, M., Fender, R. P., Tasse, C., et al. 2019, *MNRAS*, 484, 1672
- Cotton, W. D., Thorat, K., Condon, J. J., et al. 2020, *MNRAS*, 495, 1271
- Cox, C. L., Gull, S. F., & Scheuer, P. A. G. 1991, *MNRAS*, 252, 558
- de Gasperin, F., Dijkema, T. J., Drabent, A., et al. 2019, *A&A*, 622, A5
- de Gasperin, F., Intema, H. T., Shimwell, T. W., et al. 2017, *Science Advances*, 3, e1701634
- Dennett-Thorpe, J., Scheuer, P. A. G., Laing, R. A., et al. 2002, *Monthly Notices of the Royal Astronomical Society*, 330, 609
- Dominik, R. M., Linhoff, L., Elsässer, D., & Rhode, W. 2021, *MNRAS*, 503, 5448
- Doria, A., Gitti, M., Ettori, S., et al. 2012, *ApJ*, 753, 47
- Fanaroff, B. L. & Riley, J. M. 1974, *MNRAS*, 167, 31P
- Fendt, C. & Yardimci, M. 2022, *The Astrophysical Journal*, 933, 71
- Fischer, J. U., Hasinger, G., Schwope, A. D., et al. 1998, *Astronomische Nachrichten*, 319, 347
- Fragile, P. C., Blaes, O. M., Anninos, P., & Salmonson, J. D. 2007, *ApJ*, 668, 417
- Gangardt, D., Steinle, N., Kesden, M., Gerosa, D., & Stoikos, E. 2021, *Phys. Rev. D*, 103, 124026
- Gaspari, M., Ruszkowski, M., & Sharma, P. 2012, *ApJ*, 746, 94
- Giri, G., Dubey, R. P., Rubinur, K., Vaidya, B., & Kharb, P. 2022, *MNRAS*, 514, 5625
- Gitti, M., Feretti, L., & Schindler, S. 2006, *A&A*, 448, 853

- Gitti, M., Giroletti, M., Giovannini, G., Feretti, L., & Liuzzo, E. 2013, *A&A*, 557, L14
- Govoni, F. & Feretti, L. 2004, *International Journal of Modern Physics D*, 13, 1549
- Greisen, E. W. 2003, in *Astrophysics and Space Science Library*, Vol. 285, *Information Handling in Astronomy - Historical Vistas*, ed. A. Heck, 109
- Gutiérrez, E. M., Combi, L., Romero, G. E., & Campanelli, M. 2023, arXiv e-prints, arXiv:2301.04280
- Hardcastle, M. J. 2008, in *Astronomical Society of the Pacific Conference Series*, Vol. 386, *Extragalactic Jets: Theory and Observation from Radio to Gamma Ray*, ed. T. A. Rector & D. S. De Young, 46
- Hardcastle, M. J. 2013, *MNRAS*, 433, 3364
- Hardcastle, M. J. & Croston, J. H. 2020, *New Astronomy Review*, 88, 101539
- Hardcastle, M. J., Croston, J. H., & Kraft, R. P. 2007, *ApJ*, 669, 893
- Harwood, J. J., Hardcastle, M. J., & Croston, J. H. 2015, *MNRAS*, 454, 3403
- Harwood, J. J., Hardcastle, M. J., Croston, J. H., & Goodger, J. L. 2013, *MNRAS*, 435, 3353
- Hjellming, R. M. & Johnston, K. J. 1981, *ApJ*, 246, L141
- Hodges-Kluck, E. J. & Reynolds, C. S. 2011, *ApJ*, 733, 58
- Hogan, M. T., Edge, A. C., Geach, J. E., et al. 2015a, *MNRAS*, 453, 1223
- Hogan, M. T., Edge, A. C., Hlavacek-Larrondo, J., et al. 2015b, *MNRAS*, 453, 1201
- Horton, M. A., Krause, M. G. H., & Hardcastle, M. J. 2020, *MNRAS*, 499, 5765
- Horton, M. A., Krause, M. G. H., & Hardcastle, M. J. 2023, *MNRAS*, 521, 2593
- Hudson, D. S., Reiprich, T. H., Clarke, T. E., & Sarazin, C. L. 2006, *Astronomy & Astrophysics*, 453, 433
- Intema, H. T., Jagannathan, P., Mooley, K. P., & Frail, D. A. 2017, *A&A*, 598, A78
- Jackson, N., Badole, S., Morgan, J., et al. 2022, *A&A*, 658, A2
- Jaffe, W. J. & Perola, G. C. 1973, *A&A*, 26, 423
- Kappes, A., Perucho, M., Kadler, M., et al. 2019, *A&A*, 631, A49
- Kharb, P., Vaddi, S., Sebastian, B., et al. 2019, *ApJ*, 871, 249
- Koay, J. Y., Macquart, J. P., Jauncey, D. L., et al. 2018, *MNRAS*, 474, 4396
- Kolokythas, K., O'Sullivan, E., Giacintucci, S., et al. 2020, *MNRAS*, 496, 1471
- Komissarov, S. S. & Gubanov, A. G. 1994, *A&A*, 285, 27
- Komossa, S., Grupe, D., Kraus, A., et al. 2023, *MNRAS*, 522, L84
- Konar, C. & Hardcastle, M. J. 2013, *MNRAS*, 436, 1595
- Kraft, R. P., Hardcastle, M. J., Worrall, D. M., & Murray, S. S. 2005, *The Astrophysical Journal*, 622, 149
- Krause, M. G. H., Shabala, S. S., Hardcastle, M. J., et al. 2019, *MNRAS*, 482, 240
- Kun, E., Gabányi, K. É., Karouzos, M., Britzen, S., & Gergely, L. Á. 2014, *MNRAS*, 445, 1370
- Laing, R. A. & Bridle, A. H. 2013, *MNRAS*, 432, 1114
- Laing, R. A. & Bridle, A. H. 2014, *MNRAS*, 437, 3405
- Lal, D. V. & Rao, A. P. 2007, *Monthly Notices of the Royal Astronomical Society*, 374, 1085
- Lalakos, A., Gottlieb, O., Kaaz, N., et al. 2022, *ApJ*, 936, L5
- Leahy, J. P. & Parma, P. 1992, in *Extragalactic Radio Sources. From Beams to Jets*, ed. J. Roland, H. Sol, & G. Pelletier, 307–308
- Leahy, J. P. & Williams, A. G. 1984, *MNRAS*, 210, 929
- Li, Y., Bryan, G. L., Ruszkowski, M., et al. 2015, *ApJ*, 811, 73
- Lister, M. L., Kellermann, K. I., Vermeulen, R. C., et al. 2003, *The Astrophysical Journal*, 584, 135
- Liu, F. K. 2004, *Monthly Notices of the Royal Astronomical Society*, 347, 1357
- Liuzzo, E., Taylor, G. B., Giovannini, G., & Giroletti, M. 2009, *A&A*, 501, 933
- Machalski, J., Jamrozy, M., Stawarz, Ł., & Weżgowiec, M. 2016, *A&A*, 595, A46
- Mahatma, V. H., Basu, A., Hardcastle, M. J., Morabito, L. K., & van Weeren, R. J. 2023, *MNRAS*, 520, 4427
- Martí, J. M., Müller, E., Font, J. A., Ibáñez, J. M. Z., & Marquina, A. 1997, *ApJ*, 479, 151
- McKean, J. P., Godfrey, L. E. H., Vegetti, S., et al. 2016, *MNRAS*, 463, 3143
- McNamara, B. R., Russell, H. R., Nulsen, P. E. J., et al. 2016, *ApJ*, 830, 79
- Merritt, D. & Ekers, R. D. 2002, *Science*, 297, 1310
- Meyer, E., Sparks, W., Georganopoulos, M., et al. 2017, *Galaxies*, 5, 8
- Morabito, L. K., Jackson, N. J., Mooney, S., et al. 2022, *A&A*, 658, A1
- Morganti, R. 2017, *Frontiers in Astronomy and Space Sciences*, 4, 42
- Morganti, R., Jurlin, N., Oosterloo, T., et al. 2021, *Galaxies*, 9, 88
- Murgia, M., Parma, P., Mack, K. H., et al. 2011, *Astronomy & Astrophysics*, 526, A148
- Nandi, S., Caproni, A., Kharb, P., Sebastian, B., & Roy, R. 2021, *ApJ*, 908, 178
- Nolting, C., Ball, J., & Nguyen, T. M. 2023, *ApJ*, 948, 25
- O'Dea, C. P., Daly, R. A., Kharb, P., Freeman, K. A., & Baum, S. A. 2009, *A&A*, 494, 471
- Offringa, A. R., McKinley, B., Hurley-Walker, N., et al. 2014, *MNRAS*, 444, 606
- O'Sullivan, E., Giacintucci, S., David, L. P., et al. 2011, *ApJ*, 735, 11
- Pearson, T. J. 1996, in *Astronomical Society of the Pacific Conference Series*, Vol. 100, *Energy Transport in Radio Galaxies and Quasars*, ed. P. E. Hardee, A. H. Bridle, & J. A. Zensus, 97
- Perucho, M., Martí, J.-M., & Quilis, V. 2019, *MNRAS*, 482, 3718
- Quici, B., Turner, R. J., Seymour, N., et al. 2022, *MNRAS*, 514, 3466
- Rubinur, K., Das, M., Kharb, P., & Honey, M. 2017, *MNRAS*, 465, 4772
- Saikia, D. J. 2022, *Journal of Astrophysics and Astronomy*, 43, 97
- Saikia, D. J. & Jamrozy, M. 2009, *Bulletin of the Astronomical Society of India*, 37, 63
- Sanderson, A. J. R., O'Sullivan, E., & Ponman, T. J. 2009, *MNRAS*, 395, 764
- Saripalli, L. & Subrahmanyan, R. 2009, *ApJ*, 695, 156
- Shabala, S. S., Ash, S., Alexander, P., & Riley, J. M. 2008, *Monthly Notices of the Royal Astronomical Society*, 388, 625
- Shabala, S. S., Jurlin, N., Morganti, R., et al. 2020, *Monthly Notices of the Royal Astronomical Society*, 496, 1706
- Shepherd, M. C. 1997, in *Astronomical Society of the Pacific Conference Series*, Vol. 125, *Astronomical Data Analysis Software and Systems VI*, ed. G. Hunt & H. Payne, 77
- Shimwell, T. W., Hardcastle, M. J., Tasse, C., et al. 2022, *A&A*, 659, A1
- Slee, O. B., Roy, A. L., Murgia, M., Andernach, H., & Ehle, M. 2001, *AJ*, 122, 1172
- Smith, K. L., Shields, G. A., Bonning, E. W., et al. 2010, *ApJ*, 716, 866
- Steenbrugge, K. C. & Blundell, K. M. 2008, *Monthly Notices of the Royal Astronomical Society*, 388, 1457
- Taffoni, G., Becciani, U., Garilli, B., et al. 2020, in *Astronomical Society of the Pacific Conference Series*, Vol. 527, *Astronomical Data Analysis Software and Systems XXIX*, ed. R. Pizzo, E. R. Deul, J. D. Mol, J. de Plaa, & H. Verkouter, 307
- Taylor, G. B., Perley, R. A., Inoue, M., et al. 1990, *The Astrophysical Journal*, 360, 41
- Tribble, P. C. 1993, *MNRAS*, 261, 57
- Turner, R. J. & Shabala, S. S. 2015, *The Astrophysical Journal*, 806, 59
- Ubertosi, F., Gitti, M., Brighenti, F., et al. 2021, *ApJ*, 923, L25
- Ubertosi, F., Gitti, M., Brighenti, F., et al. 2023, *ApJ*, 944, 216
- Ubertosi, F., Schellenberger, G., O'Sullivan, E., et al. 2024, *ApJ*, 961, 134
- van Diepen, G., Dijkema, T. J., & Offringa, A. 2018, *DPPP: Default Pre-Processing Pipeline*, *Astrophysics Source Code Library*, record ascl:1804.003
- van Haarlem, M. P., Wise, M. W., Gunst, A. W., et al. 2013, *A&A*, 556, A2
- van Weeren, R. J., Shimwell, T. W., Botteon, A., et al. 2021, *A&A*, 651, A115
- van Weeren, R. J., Williams, W. L., Hardcastle, M. J., et al. 2016, *ApJS*, 223, 2
- von Fellenberg, S. D., Janssen, M., Davelaar, J., et al. 2023, *A&A*, 672, L5
- Whitehead, H. W. & Matthews, J. H. 2023, *MNRAS*, 523, 2478
- Williams, W. L., van Weeren, R. J., Röttgering, H. J. A., et al. 2016, *MNRAS*, 460, 2385
- Wolowska, A., Kunert-Bajraszewska, M., Mooley, K. P., et al. 2021, *ApJ*, 914, 22